

1
2 **Deep Learning for Daily 2-m Temperature Downscaling**
3

4 **Shuyan Ding¹, Xiefei Zhi¹, Yang Lyu¹, Yan Ji¹, and Weijun Guo²**

5 1. Key Laboratory of Meteorology Disaster, Ministry of Education (KLME)/Joint International
6 Research Laboratory of Climate and Environment Change (ILCEC)/Collaborative Innovation
7 Center on Forecast and Evaluation of Meteorological Disasters (CIC-FEMD), Nanjing
8 University of Information Science and Technology, Nanjing, Jiangsu 210044, China.

9 2. Xiamen Air Traffic Management Station of China Civil Aviation, Xiamen, Fujian 361006,
10 China

11 Corresponding author: Xiefei Zhi (zhi@nuist.edu.cn)

12 **Key Points:**

- 13 • This paper presents a novel deep learning downscaling method, UNR-Net, capable of
14 downscaling daily 2-m temperature by a factor of 10
- 15 • The overall performance of the UNR-Net method surpasses the U-Net method and linear
16 regression method
- 17 • The 12 components-based error decomposition method is proposed to analyze the error
18 source of different models.
19

20

Abstract

21 This study proposes a novel method, which is a U-shaped convolutional neural network that
22 combines non-local attention mechanisms, Res2net residual modules, and terrain information
23 (UNR-Net). The original U-Net method and the linear regression (LR) method are conducted as
24 benchmarks. Generally, the UNR-Net has demonstrated promise in performing a 10x
25 downscaling for daily 2-m temperature over North China with lead times of 1–7 days and shows
26 superiority to the U-Net and LR methods. To be specific, U-Net and UNR-Net demonstrate
27 higher Nash-Sutcliffe Efficiency coefficient (NSE) values compared to LR by 0.052 and 0.077,
28 respectively. The corresponding improvements in pattern correlation coefficient are 0.013 and
29 0.016, while the root mean square error values are higher by 0.22 and 0.338, respectively.
30 Additionally, the structural similarity index metric is higher by 0.033 and lower by 0.015.
31 Furthermore, regions with significant errors are primarily distributed in complex terrain areas
32 such as the Taihang Mountains, where UNR-Net exhibits noticeable improvements. In addition,
33 the 12 components-based error decomposition method is proposed to analyze the error source of
34 different models. Generally, the smallest errors are observed during the summer season and the
35 sequence error component is proven to be the main source error of 2-m temperature forecasts.
36 Furthermore, UNR-Net consistently demonstrates the lowest errors among all 12 error
37 components. Therefore, combining the numerical weather prediction model and deep learning
38 method is very promising in downscaling temperature forecasts and can be applied to routine
39 forecasting of other atmospheric variables in the future.

Plain Language Summary

41 This research proposes a new method for downscaling using deep learning. The method uses a
42 specific type of neural network called UNR-Net, which combines attention mechanisms, residual
43 modules, and terrain information. The performance of UNR-Net is compared to two other
44 methods: U-Net and LR. In the study, UNR-Net shows promise in performing a 10x downscaling
45 of the daily 2-m temperature in North China. The UNR-Net demonstrates the best overall
46 performance among all the comprehensive indicators (NSE, pattern correlation coefficient, root
47 mean square error, and structural similarity index metric). Errors in the predictions are mainly
48 found in complex terrain areas like the Taihang Mountains, but UNR-Net shows noticeable
49 improvements in these regions. The study also proposes a 12 components-based error
50 decomposition method to analyze the error sources of different models. All in all, it is found that

51 the smallest errors are observed during the summer season and the main source error is the
52 sequence error component. Additionally, when considering lead times of 1–7 days, UNR-Net
53 consistently shows the lowest errors among all 12 error components. Based on these findings,
54 combining numerical weather prediction models with deep learning methods holds great promise
55 for generating high-resolution temperature forecasts.

56 **1. Introduction**

57 Temperature is a meteorological element closely related to human life. With the advancement of
58 society, there is an increasing demand for high-resolution temperature forecasts. However, in the
59 present era, the resolution of numerical models is limited due to factors such as computational
60 costs, scale sensitivity, and mismatches (Rind et al., 1992), which pose challenges in meeting the
61 requirements of practical applications and scientific research. (Roberts et al., 2018; Feser et al.,
62 2011; Wilby & Wigley, 1997). Therefore, downscaling methods have emerged.

63 These methods utilize appropriate refinement processes to infer meteorological element
64 information at local scales based on the available low-resolution data (Höhlein et al., 2020). Due
65 to the complexity of spatiotemporal characteristics, downscaling remains a challenging and
66 intricate problem. Over the past few decades, various downscaling techniques have been
67 proposed, including simple downscaling, dynamical downscaling (Jing et al. 2022; Wang et al.
68 2021), and statistical downscaling (Sharifi et al., 2019; Fowler et al., 2007). Among these,
69 statistical downscaling exhibits a distinct advantage due to its high accuracy, excellent
70 scalability, and lower computational resource requirements (Kim & Barros 2002; Frei et al.,
71 2003; Hagemann et al., 2004; Ji et al., 2023a; Mannig et al., 2013).

72 In the past few decades, numerous advancements have been made in statistical downscaling
73 techniques. Although traditional statistical approaches can to some extent enhance the resolution,
74 they still have limitations in utilizing spatial and temporal dependencies, resulting in limited
75 fitting capabilities (Chen et al., 2018; Wilby et al., 1998; He et al., 2016b). With the advent of
76 the big data era, deep learning has the potential to discover features in high-dimensional data and
77 capture the underlying nonlinear relationships between various meteorological variables (Yuan et
78 al., 2020). It shows promise in terms of both accuracy and efficiency, surpassing previous
79 methods (Höhlein et al., 2020). However, the use of deep learning methods in the field of
80 meteorological downscaling is still in its early stages and faces challenges such as inadequate

81 description of complex features and poor performance in extreme events (Baño-Medina et al.,
82 2020; Ji et al., 2022; Ji et al., 2023b; Vandal et al., 2019). Therefore, further practical exploration
83 and research are needed to address these issues.

84 Presently, the field of deep learning offers numerous techniques that are well-suited for
85 addressing challenges in the domain of downscaling. Due to its ability to incorporate receptive
86 fields of varying sizes, U-Net has achieved success in semantic segmentation tasks (Ronneberger
87 et al., 2015). Subsequently, it has also shown promising performance in tasks such as forecast
88 calibration (Han et al., 2021; Zhu et al., 2022) and downscaling (Doury et al., 2023; Sha et al.,
89 2020). However, when U-Net is employed for downscaling end-to-end tasks, the accuracy and
90 practical effectiveness of the results can still be further improved through existing techniques.

91 Mnih et al. (2014) achieved impressive results and gained widespread attention by incorporating
92 attention mechanisms into convolutional neural networks for image processing tasks. Since then
93 various attention mechanisms have emerged (Hu et al., 2018; Woo et al. 2018), and it has also
94 found applications in downscaling (Park et al., 2022; Jing et al., 2022; Gerges et al., 2022). In
95 theory, deeper networks have larger receptive fields, allowing them to integrate more
96 information and potentially achieve better results. However, training deep networks can
97 encounter challenges such as vanishing/exploding gradients and degradation (Pan et al., 2019).
98 The Residual Network (ResNet), proposed by He et al. (2016a) successfully addressed the issue
99 of network degradation. Subsequently, numerous studies have discussed the concept of residuals
100 and proposed various variants (Xie et al., 2017; Huang et al., 2017; Veit et al., 2016).

101 Furthermore, regarding the utilization of meteorological variables, apart from studies that solely
102 utilize the meteorological variables at the downscaled scale (Kumar et al., 2021; Höhle et al.,
103 2020), some researchers have taken into account the physical significance and constraints of
104 meteorological variables by incorporating terrain data into neural networks (Sha et al., 2020).
105 But most studies that utilize multivariate data simply incorporate auxiliary data by stacking
106 channels during input. This approach fails to effectively utilize higher-resolution auxiliary
107 information compared to the target resolution, and there is also a lack of discussion regarding the
108 optimal utilization of auxiliary information.

109 As a result, we propose a novel U-shaped convolutional neural network called UNR-Net, which
110 integrates a nonlocal attention mechanism (Wang et al., 2018), Res2net (Gao et al., 2019), and
111 terrain information for downscaling temperature. A non-local attention mechanism can allocate

112 importance to each position from a global perspective, considering the correlations between
113 high-resolution observational data and low-resolution forecast data while disregarding distance.
114 Res2net modules serve the purpose of not only mitigating model degradation issues but also
115 efficiently coupling multiple receptive field sizes. We employ multiple convolutional operations
116 to progressively decrease the resolution of the terrain data while increasing the number of
117 channels and then fuse these products into the network through skip connections, which can not
118 only adjust the feature map size of the high-resolution terrain data for easier input, but also
119 preserve the high-resolution information of the terrain data, and control the proportion of terrain
120 information in the network during feature extraction and downscaling. Additionally, in the
121 downscaling part of the network, a combination of nearest-neighbor interpolation and
122 convolution was utilized for upsampling (Dong et al., 2016), which can avoid the “checkerboard
123 effect” caused by transpose convolution (Gauthier, 2014; Dumoulin et al., 2017).

124 The evaluation phase of the model after the modeling process is crucial. For model evaluation,
125 the performance of UNR-Net is compared with LR, the original U-Net, and low-resolution
126 forecast data with the comprehensive evaluation metrics NSE, pattern correlation coefficient
127 (PCC), root mean square error (RMSE), and structural similarity index metric (SSIM). Still, the
128 comprehensive evaluation metrics can only assess the overall performance of methods from
129 various perspectives, which often lack detailed assessment and specific physical significance.
130 Error decomposition, on the other hand, can provide a further evaluation of the results and
131 enhance the interpretability of the methods (Hodson et al., 2021). Initially, the mean squared
132 error (MSE) is decomposed into four seasons, and then the error for each season is further
133 decomposed into three components, enabling a more detailed and specific analysis. The
134 remainder of this paper follows the following structure. Section 2 describes the utilized data.
135 Section 3 outlines the methods employed. Section 4 analyzes the performance of the three
136 downsampling methods. Finally, a summary and discussion are presented in Section 5.

137 **2. Data**

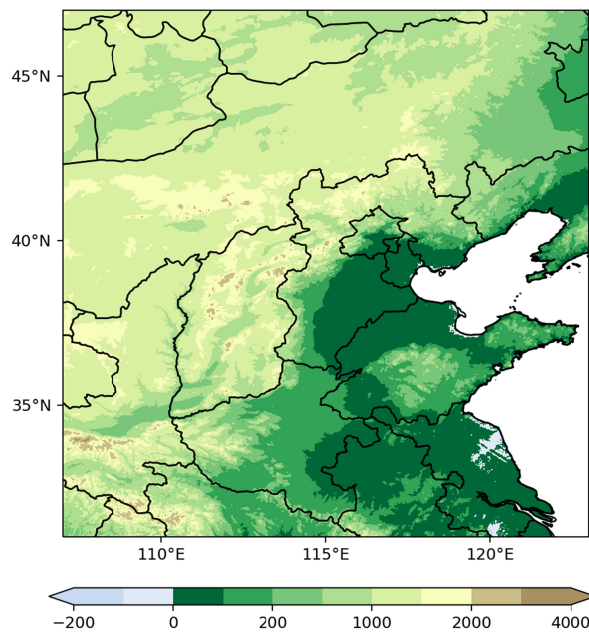
138 The research area of this paper covers the geographical coordinates of (107° to 122.9°E, 31.1° to
139 47°N). The eastern part of the region is characterized by low-lying terrain and proximity to the
140 ocean, while the western part features higher elevations and is situated inland. The region is
141 predominantly mountainous with hilly terrain, exhibiting significant topographical variations.

142 Due to the significant impact of elevation on 2-m temperature and the region's importance as an
143 agricultural area, downscaled modeling in such complex terrain is highly challenging yet holds
144 substantial practical significance.

145 The forecast data used in this study is sourced from the Global Ensemble Forecasting System
146 (GEFS) of the National Centers for Environmental Prediction (NCEP). The model resolution is
147 $0.25^\circ \times 0.25^\circ$, and the data covers the geographical region of (105° to 124°E , 30° to 49°N). The
148 dataset spans the period from 1 January 2010 to 31 December 2019, with daily initializations at
149 0000 UTC. The experiment incorporates 2-m temperature data with lead times of 1–7 days.

150 In this study, the observational data utilized the ERA5-Land dataset provided by the European
151 Centre for Medium-Range Weather Forecasts (ECMWF). The dataset had a resolution of $0.1^\circ \times$
152 0.1° and covered the time period from 2 January 2010 to 7 January 2020, with a focus on daily 2-
153 m temperature data at 0000 UTC and covers the geographical region of (105° to 124.9°E , 29.1°
154 to 49°N).

155 The topographic data utilized in this study was derived from the ETOPO1 dataset provided by
156 the National Oceanic and Atmospheric Administration (NOAA). The dataset has a resolution of
157 $1' \times 1'$ and covers the geographical region of (105° to $124^\circ 59'\text{E}$, $29^\circ 1'$ to -49°N) (Figure 1).



158

159 **Figure 1.** Study domain. The color bar represents the altitude of the terrain (m).

160 **3. Methods**

161 In this study, a total of three methods were employed to perform a 10x downscaling on the North
 162 China region. The three methods used were LR, U-Net, and UNR-Net. The first method, LR, is a
 163 traditional downscaling approach. It involves performing bilinear interpolation on the low-
 164 resolution forecast data and then applying linear regression. The second method is the
 165 unmodified original U-Net, where the upsampling process utilizes transpose convolutions. The
 166 third method is a modified version of the U-Net that combines non-local attention with Res2net
 167 residual modules. Additionally, it incorporates terrain information to enhance the performance of
 168 the model. These three methods utilize the data that has undergone data preprocessing as
 169 described in Section 3.1, and these three methods share the same training set, validation set, and
 170 test set. The two deep learning methods both employ an end-to-end approach, where the
 171 networks simultaneously perform the calibration and downscaling tasks. Additionally, the
 172 training process for both networks is identical and follows a supervised learning approach. The
 173 Adam optimizer is used for training in both cases (Kingma & Ba, 2017). The loss function used
 174 is MSE, defined as follows:

$$MSE = \frac{1}{N} \sum_{i=1}^N (y_i - y'_i)^2, \#(1)$$

175 where N represents the number of grid points in a batch, i represents the grid point position, y_i
 176 represents the ground truth values, and y'_i , represents the predicted values. The learning rate is set
 177 to 0.001, and it is decayed every 20 steps with a decay rate of 0.5. To avoid overfitting, early
 178 stopping is implemented to determine the stopping epoch. Finally, an evaluation is conducted on
 179 the results of the three methods, which includes the error between the high-resolution
 180 downscaled results and high-resolution observation, as well as the error between the low-
 181 resolution observation and the low-resolution forecast data after second-order conservative
 182 remapping scheme (Jones, 1999). Subsequently, an error decomposition is performed to further
 183 analyze the performance of the three methods.

184 **3.1 Data Preprocessing**

185 First, data processing is conducted on the forecast data. The forecast data has a resolution of
 186 $0.25^\circ \times 0.25^\circ$, and due to the downscaling factor of 10 used in the experiment, the resolution of
 187 the observational data is $0.1^\circ \times 0.1^\circ$. Therefore, the first step is to perform a second-order

188 conservative remapping scheme (Jones, 1999) to adjust the resolution of the forecast data to $1^\circ \times$
189 1° . Due to the absence of observational data for the oceanic region, the oceanic part of the
190 forecast data is assigned empty values. Then, the land data is standardized using the following
191 formula:

$$x_{new} = \frac{x - \mu}{\sigma}, \#(2)$$

192 where x represents the previous value of the data, x_{new} represents the new value of the data, μ
193 represents the mean of the respective matrix, and σ represents the variance. Afterward, the
194 oceanic region is filled using the nearest-neighbor interpolation method, as described by the
195 formula:

$$f(i) = f(i_{nearest}), \#(3)$$

196 where i represents the grid point location, $i_{nearest}$ represents the closest grid point location to i ,
197 $f(i_{nearest})$ represents the value of the nearest grid point, and $f(i)$ represents the value of the
198 grid point i . By applying the mentioned processing to the forecast data, the low-resolution
199 forecast data is obtained.

200 Next, the observational data are processed in a similar manner as the forecast data, including
201 standardization and nearest-neighbor interpolation for the oceanic regions. This results in
202 obtaining the high-resolution observational data.

203 Both the low-resolution forecast data and the high-resolution observational data are divided into
204 training sets, validation sets, and testing sets. The training set consists of data with forecast start
205 dates from 1 January 2010 to 31 December 2017. The validation set comprises data with forecast
206 start dates from 1 January 2017 to 31 December 2018. Lastly, the testing set includes data with
207 forecast start dates from 1 January 2018 to 31 December 2019.

208 Finally, the terrain data is processed using the same methods as applied to the forecast data,
209 including standardization and nearest-neighbor interpolation for the oceanic regions. This results
210 in obtaining the high-resolution terrain data.

211 3.2 Downscaling methods

212 3.2.1 LR

213 First, the low-resolution forecast data is subjected to bilinear interpolation. Bilinear interpolation
214 involves performing linear interpolation in two directions. The formulas for bilinear interpolation
215 are as follows:

$$f(X_r, Y_a) \approx \frac{X_b - X_r}{X_b - X_a} f(X_a, Y_a) + \frac{X_r - X_a}{X_b - X_a} f(X_b, Y_a), \#(4)$$

$$f(X_r, Y_b) \approx \frac{X_b - X_r}{X_b - X_a} f(X_a, Y_b) + \frac{X_r - X_a}{X_b - X_a} f(X_b, Y_b), \#(5)$$

216 where $f(X_a, Y_a)$, $f(X_b, Y_a)$, $f(X_a, Y_b)$, and $f(X_b, Y_b)$ represent the values of the four points in the
217 respective directions. X_a , X_b , Y_a , and Y_b represent the positions on the coordinate axes, while
218 $f(X_r, Y_a)$ and $f(X_r, Y_b)$ represent the points obtained through linear interpolation in the x-
219 direction. After obtaining $f(X_r, Y_a)$ and $f(X_r, Y_b)$, linear interpolation is performed in the y-
220 direction to obtain the value of the unknown point as follows:

$$f(X_r, Y_r) \approx \frac{Y_b - Y_r}{Y_b - Y_a} f(X_r, Y_a) + \frac{Y_r - Y_a}{Y_b - Y_a} f(X_r, Y_b), \#(6)$$

221 where $f(X_r, Y_r)$ represents the value of the unknown point. As a result, we obtain the forecast
222 data with a resolution of $0.1^\circ \times 0.1^\circ$. Next, linear regression is applied to the forecast data,
223 following the formula:

$$y_t = a + bx_t, \#(7)$$

224 where y_t represents the predicted result, x_t represents the values for linear regression, and a and
225 b are the coefficients of the linear regression. The coefficients a and b in linear regression are
226 calculated using the following formulas:

$$a = \bar{y} - b\bar{x}, \#(8)$$

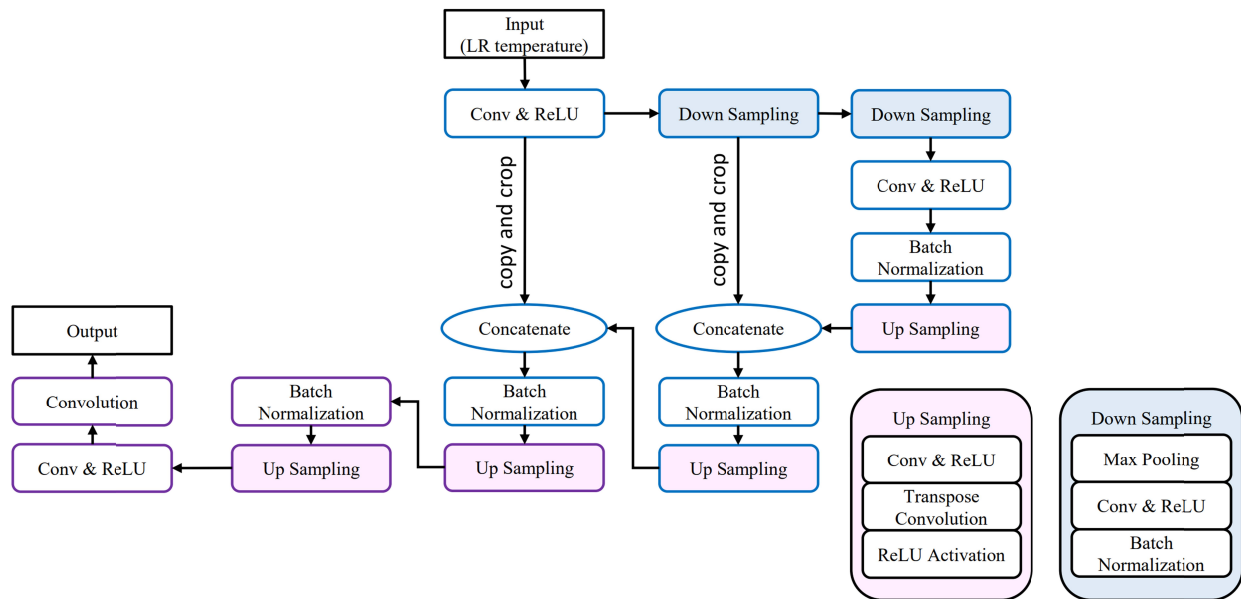
$$b = \frac{\sum_{t=1}^n x_t y_t - n\bar{x}\bar{y}}{\sum_{t=1}^n x_t^2 - n\bar{x}^2}, \#(9)$$

227 where x_t represents the forecast data in the training set, y_t represents the observational data in
228 the training set, \bar{x} represents the mean of the forecast data in the training set, and \bar{y} represents the
229 mean of the observational data in the training set. After obtaining the regression coefficients a

230 and b for each grid point, the regression equation is applied to the testing set. This process yields
 231 the downscaled results using the LR method for the testing set.

232 3.2.2 U-Net

233 The U-Net is a convolutional neural network architecture with a U-shaped structure that was first
 234 introduced in the field of semantic segmentation (Ronneberger et al. 2015). Its encoder-decoder
 235 structure is well-suited for handling pixel-level problems and is also well-suited for processing
 236 grid-based meteorological data. The downscaling U-Net architecture employed in this study
 237 employs multiple upsampling operations in the decoder section, iteratively generating feature
 238 maps at the desired target resolution (Figure 2).



239
 240 **Figure 2.** U-Net architecture. The rectangular box with right angles represents the data, while the
 241 rounded rectangles and ellipses represent different operations or functions. The text inside the
 242 rounded rectangles and ellipses indicates the name of the respective operation or function. The
 243 solid arrows indicate the flow of data. The blue box represents the feature extraction section,
 244 while the purple box represents the downscaling section.

245 The downscaling U-Net architecture in this paper consists of two components: the blue box
 246 representing the feature extraction section and the purple box representing the downscaling
 247 section. Placing the upsampling process after the feature extraction section can reduce
 248 computational load without compromising the accuracy of the results. The feature extraction

249 section accepts input data of low resolution for forecasting. The structure of the feature
 250 extraction section consists of the left encoder part and the right decoder part. Downsampling is a
 251 critical process in the encoder, and the downsampling module comprises pooling, convolution,
 252 and activation operations. Through the downsampling module, the size of the feature maps is
 253 halved, while the number of channels is doubled compared to the original. Upsampling is an
 254 essential process in the decoder, and the upsampling module consists of convolution, activation,
 255 transposed convolution, and activation operations. Through the upsampling module, the size of
 256 the feature maps is doubled, while the number of channels is halved compared to the original.
 257 Then the feature maps of the same size are concatenated through skip connections. Skip
 258 connections allow for the integration of information from different scales, thereby enhancing the
 259 network's ability to capture complex patterns and improve its fitting capability. The number of
 260 convolutional kernels in each layer of the feature extraction section is {16, 32, 64, 64, 64, 32, 32,
 261 16}. The downsampling section includes two upsampling processes. The order of operations in
 262 the upsampling module is consistent with the feature extraction section. However, in the final
 263 upsampling module, the size of the feature maps is increased by a factor of 5. After the
 264 upsampling, batch normalization, convolution, and activation operations in the downsampling
 265 section, the high-resolution downscaled results are obtained. The number of convolutional
 266 kernels in each layer of the feature extraction section is {16, 16, 16, 16, 16, 16, 1}. The
 267 relationship to control the output feature map size in convolutional operations within the network
 268 can be represented as,

$$o = \left\lfloor \frac{i + 2p - k}{s} \right\rfloor + 1. \#(10)$$

269 The relationship to control the output feature map size in transpose convolutional operations can
 270 be represented as:

$$o = s(i - 1) + k - 2p, \#(11)$$

271 where o represents the size of the output feature map, i represents the size of the input feature
 272 map, p represents the padding size, k represents the size of the convolutional kernel, and s
 273 represents the stride of the convolution operation. The activation function used is Rectified
 274 Linear Unit (ReLU) (Glorot et al., 2011), which is widely used and highly effective in regression
 275 problems. Its formula is as follows:

$$\text{ReLU}(x_i) = \max(0, x_i), \#(12)$$

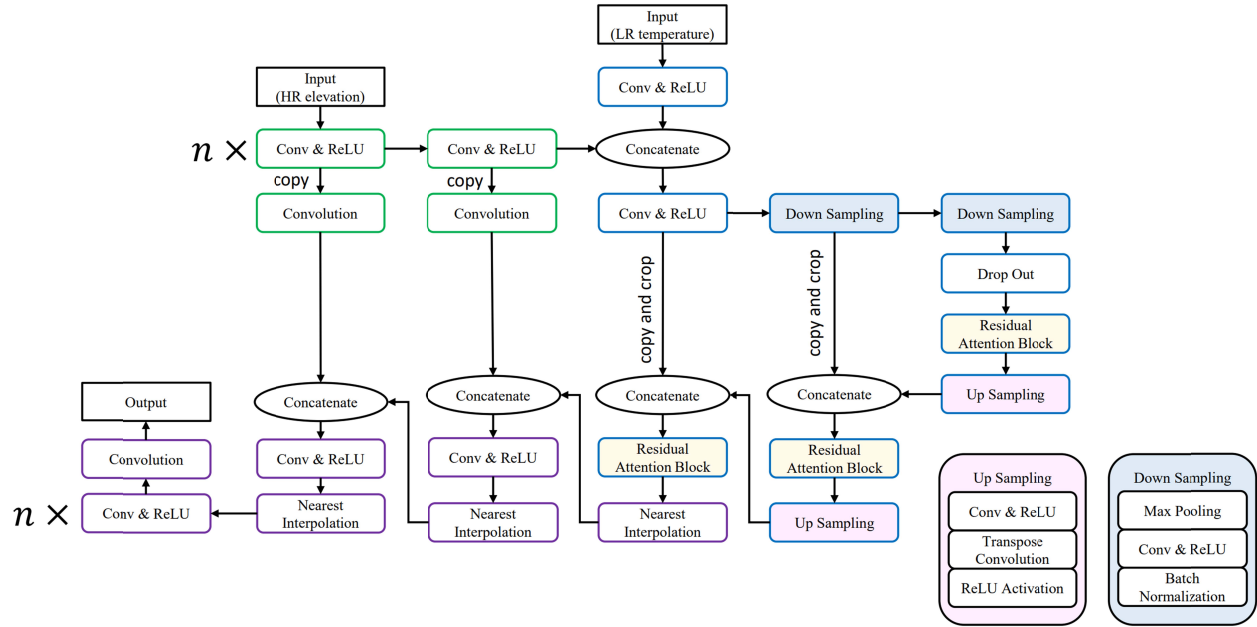
276 where, x_i represents the elements of the feature map to the activation function. Batch
 277 normalization is also employed in the network. Batch normalization helps alleviate the problem
 278 of internal covariate shifts during the training process (Ioffe & Szegedy, 2015). It stabilizes the
 279 learning process by normalizing the inputs of each layer within a mini-batch and has shown good
 280 performance in accelerating the training of various deep learning models and regularization
 281 (Silver et al., 2017). The formula for batch normalization is as follows;

$$\text{BN}(X) = \frac{X - E[X]}{\sqrt{\text{Var}[X] + \epsilon}} \times \gamma + \beta, \#(13)$$

282 where γ and β are trainable parameters, ϵ is a small constant value, X represents the feature map
 283 matrix, $E[X]$ is the mean of the feature map matrix X , and $\text{Var}[X]$ is the variance of the feature
 284 map matrix X .

285 3.2.3 UNR-Net

286 The UNR-Net consists of three components: the auxiliary information processing section, the
 287 feature extraction section, and the downscaling section (Figure 3). The auxiliary information
 288 processing section receives high-resolution terrain data and outputs to both the feature extraction
 289 section and the downscaling section. The feature extraction section takes inputs from the low-
 290 resolution forecast data and the auxiliary information processing section, and outputs to the
 291 downscaling section. The downscaling section receives inputs from both the auxiliary
 292 information processing section and the feature extraction section, ultimately generating high-
 293 resolution downscaled results.

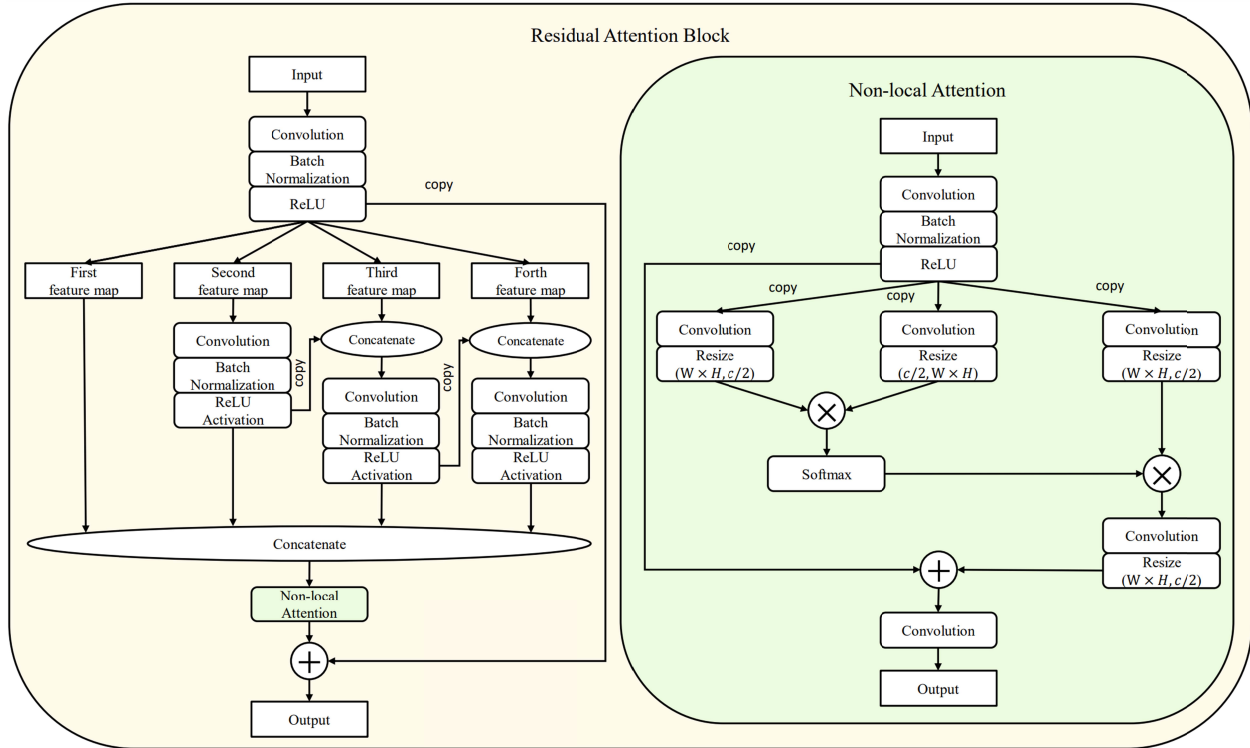


294

295 **Figure 3.** UNR-Net architecture. The green box represents the auxiliary information processing
 296 section, the blue box represents the feature extraction section, and the purple box represents the
 297 downscaling section. The rest of the instructions are the same as in Figure 2.

298 The auxiliary information processing section accepts high-resolution auxiliary data, and the
 299 resolution of the auxiliary data can be higher than the target resolution of the downscaling task.
 300 Because in this section, we control the size of the output feature maps by utilizing (Equation 9),
 301 the result is a gradual reduction in the dimensions of the feature maps. In this task, the resolution
 302 of the terrain data is 60 times higher than that of the low-resolution forecast data. In this network,
 303 the size of the feature maps gradually decreases by factors of 2, 3, 5, and 2. Specifically, the data
 304 that undergoes a total reduction of 6 and 30 times is input into the downscaling part, while the
 305 data that undergoes a total reduction of 60 times is input into the feature extraction part. The
 306 number of convolutional kernels in this part is $\{8, 8, 8, 8, 6\}$, and after the first and second
 307 copies, the number of convolutional kernels for the subsequent convolution operations is $\{1, 1\}$.

308 The difference between the feature extraction part in this section and the feature extraction part
 309 in the downscaling U-Net described in Section 3.2.2, is the utilization of dropout layers to
 310 prevent alleviate overfitting (Srivastava et al., 2014), the removal of some batch normalization
 311 operations (Li et al. 2019), and the addition of residual attention modules. The addition of the
 312 residual attention modules is one of the key improvements in the network.



313

314 **Figure 4.** The Residual Attention Module. The numbers within the parentheses for the resize
 315 operation represent the shape of the output feature map, and the \otimes represents matrix
 316 multiplication.

317 This module primarily consists of the Res2net module (Gao et al., 2019) and a non-local
 318 attention mechanism (Wang et al., 2018) (Figure 4). The Res2net module divides the feature map
 319 into four segments along the channel dimension and processes them separately. This approach
 320 enables more efficient integration of multiple receptive field sizes, allowing the model to capture
 321 information from different scales effectively. Additionally, it helps prevent model degradation,
 322 ensuring stable and robust performance. The nonlocal attention mechanism is a spatially
 323 sensitive attention mechanism. Within the attention part of the module, the input is first
 324 replicated four times for separate operations. One of the replicas is used for residual connection,
 325 while the other two replicas are used to generate attention weights. These attention weights are
 326 then multiplied with the fourth replica, resulting in a feature map that emphasizes important
 327 regions. During the generation of attention weights, the module performs matrix multiplication
 328 on the resized feature maps to produce the attention weights, similar to the process of generating
 329 a covariance matrix. These attention weights are then activated using the softmax
 330 function, given by the formula:

$$\text{Softmax}(z_i) = \frac{e^{z_i}}{\sum_{c=1}^C e^{z_c}}, \#(14)$$

331 where z_i represents the elements of the attention weight matrix, and C represents the total
 332 number of elements in the attention weight matrix. Finally, the attention-weighted feature map is
 333 obtained by multiplying it element-wise with the fourth copy of the feature map that underwent
 334 convolution and resizing operations. This results in a feature map where the importance is
 335 allocated based on the attention weights. Therefore, this non-local attention mechanism can
 336 allocate the importance of each position in the feature map from a global perspective,
 337 considering the correlation between high-resolution observational data and low-resolution
 338 forecast data, while ignoring the spatial distance and capturing the interactions across different
 339 locations. The distinction between the downscaling components of UNR-Net and U-Net lies in
 340 the source of data and the methodology employed for upsampling. The downscaling section of
 341 this network not only receives inputs from the feature extraction part but also incorporates inputs
 342 from the auxiliary information processing section after each upsampling step. These input feature
 343 maps have a smaller receptive field, allowing the network to incorporate information from a
 344 smaller scale and enhance its fitting capability. Moreover, the upsampling method in the
 345 downscaling section of UNR-Net has been changed from transpose convolution to a combination
 346 of nearest-neighbor interpolation and convolution. This change was made to address the issue of
 347 checkerboard artifacts that can be introduced by transpose convolution, which can potentially
 348 affect the practical utility of the network (Dumoulin et al., 2017). The combination of nearest-
 349 neighbor interpolation and convolution for upsampling helps to avoid the occurrence of
 350 checkerboard artifacts without compromising result accuracy. The formula for nearest-neighbor
 351 interpolation is as follows:

$$\text{srcX} = \text{dstX} \times \frac{\text{srcWidth}}{\text{dstWidth}}, \#(15)$$

$$\text{srcY} = \text{dstY} \times \frac{\text{srcHeight}}{\text{dstHeight}}, \#(16)$$

352 where dstX and dstY represent the coordinates of the enlarged feature map's grid points;
 353 dstWidth and dstHeight represent the length and width of the enlarged feature map; srcX and
 354 srcY represent the coordinates of the original feature map's grid points; srcWidth and
 355 srcHeight represent the length and width of the original feature map.

356 The network shares the same operations and parameters as the U-Net, except for the differences
357 mentioned above.

358 3.3 Evaluation metrics

359 We have employed six evaluation methods to assess the strengths and weaknesses of the three
360 approaches from various perspectives. The six evaluation methods are the NSE (Nash et al.,
361 1970), PCC, RMSE, SSIM, Root Mean Square Error Skill Score (RMSESS), and MSE. Their
362 formulas are given as follows:

$$NSE = 1 - \frac{\sum_{i=1}^n (o_i - f_i)^2}{\sum_{i=1}^n (o_i - \bar{o})^2}, \#(17)$$

$$PCC = \frac{\sum_{i=1}^m (f_i - \bar{f})(o_i - \bar{o})}{\sqrt{\sum_{i=1}^m (o_i - \bar{o})^2 (f_i - \bar{f})^2 \sum_{i=1}^m (o_i - \bar{o})^2}}, \#(18)$$

$$RMSE = \sqrt{\frac{1}{m} \sum_{i=1}^m (f_i - o_i)^2}, \#(19)$$

$$SSIM = \frac{(2\bar{o}\bar{f} + C_1)(2\sigma_{of} + C_2)}{(\bar{f}^2 + \bar{o}^2 + C_1)(\sigma_f^2 + \sigma_o^2 + C_2)}, \#(20)$$

$$RMSESS = \frac{RMSE_{ref} - RMSE}{RMSE_{ref}}, \#(21)$$

$$MSE = \frac{1}{m} \sum_{i=1}^m (f_i - o_i)^2, \#(22)$$

363 where o represents the observation; f represents the forecast; n represents the number of time
364 steps; m represents the number of grid points; \bar{o} and \bar{f} represent the mean of observations and
365 forecasts (in the case of NSE , it represents the mean over all time steps for a grid point, and in
366 other formulas, it represents the mean over all grid points for a time step); respectively; σ_o is the
367 standard deviation of observations; σ_f is the standard deviation of forecasts; σ_{of} is the
368 covariance between observations and forecasts; C_1 and C_2 are constants. Among the six
369 evaluation metrics, higher values indicate better performance, except for RMSE and MSE, in

370 which a lower value is desirable. *NSE* reflects the fitting effect of the downscaled results to the
 371 observations (Gerges et al., 2022). *PCC* measures the correlation between the forecast field and
 372 the observation field. *RMSE* represents the absolute error between the forecast values and the
 373 observed values. *SSIM* measures the similarity between the forecast field and the observation
 374 field, which is more in line with human visual perception. *RMSESS* quantifies the comparison
 375 between two methods. *MSE*, as an absolute error, can amplify the *RMSE*.

376 3.4 Error decomposition

377 While comprehensive evaluation metrics allow for the quantification of model performance from
 378 various perspectives, they often lack interpretability and provide limited guidance for model
 379 improvement (Zhu et al., 2022). Error decomposition, on the other hand, enables the breakdown
 380 of absolute errors into interpretable components, facilitating a more in-depth evaluation (Hodson
 381 et al., 2021).

382 First, the model error ϵ is defined as,

$$\epsilon = \mathbf{f} - \mathbf{o}, \#(23)$$

383 where \mathbf{f} represents a downscaled results vector with n values, and \mathbf{o} represents an observation
 384 vector with n values.

385 The error can be divided into four components representing the four seasons,

$$\epsilon = \epsilon_1 + \epsilon_2 + \epsilon_3 + \epsilon_4, \#(24)$$

$$= \delta_1 \epsilon + \delta_2 \epsilon + \delta_3 \epsilon + \delta_4 \epsilon, \#(25)$$

386 where 1, 2, 3, and 4 represent the four seasons (spring, summer, autumn, and winter,
 387 respectively), and δ is a matrix of the same shape as ϵ , consisting of elements 0 and 1,

$$\delta_{ij} = \begin{cases} 1 & \text{if } \epsilon_i \in \text{season } j \\ 0 & \text{otherwise} \end{cases}. \#(26)$$

388 So, the *MSE* can be decomposed as follows:

$$MSE(\epsilon) = MSE(\epsilon_1 + \epsilon_2 + \epsilon_3 + \epsilon_4), \#(27)$$

$$= \frac{1}{n} \sum_{i=1}^n (\epsilon_{1i} + \epsilon_{2i} + \epsilon_{3i} + \epsilon_{4i})^2, \#(28)$$

$$\begin{aligned}
&= \frac{1}{n} \sum_{i=1}^n (\epsilon_{1i})^2 + \frac{1}{n} \sum_{i=1}^n (\epsilon_{2i})^2 + \frac{1}{n} \sum_{i=1}^n (\epsilon_{3i})^2 + \frac{1}{n} \sum_{i=1}^n (\epsilon_{4i})^2 \\
&+ \frac{2}{n} \sum_{i=1}^n (\epsilon_{1i} \cdot \epsilon_{2i}) + \frac{2}{n} \sum_{i=1}^n (\epsilon_{3i} \cdot \epsilon_{4i}) + \frac{2}{n} \sum_{i=1}^n (\epsilon_{1i} + \epsilon_{2i}) \cdot (\epsilon_{3i} + \epsilon_{4i}). \#(29)
\end{aligned}$$

389 Since the errors for the four seasons are orthogonal to each other, the term $\frac{2}{n} \sum_{i=1}^n (\epsilon_{1i} \cdot \epsilon_{2i}) +$
390 $\frac{2}{n} \sum_{i=1}^n (\epsilon_{3i} \cdot \epsilon_{4i}) + \frac{2}{n} \sum_{i=1}^n (\epsilon_{1i} + \epsilon_{2i}) \cdot (\epsilon_{3i} + \epsilon_{4i})$ equals zero. According to Hodson et al. (2021),
391 each MSE can be decomposed into three components: Bias, Sequence, and Distribution.
392 Therefore, it follows,

$$\begin{aligned}
MSE(\epsilon) &= Bias(\epsilon_1)^2 + Sequence(\epsilon_1) + Distribution(\epsilon_1) \\
&+ Bias(\epsilon_2)^2 + Sequence(\epsilon_2) + Distribution(\epsilon_2) \\
&+ Bias(\epsilon_3)^2 + Sequence(\epsilon_3) + Distribution(\epsilon_3) \\
&+ Bias(\epsilon_4)^2 + Sequence(\epsilon_4) + Distribution(\epsilon_4). \#(31)
\end{aligned}$$

393 The Bias component quantifies the model's ability to accurately replicate the mean of the
394 observations. The Sequence component measures the model's ability to accurately reproduce
395 temporal sequences of events. The Distribution component quantifies the model's ability to
396 accurately replicate the distribution of the observations. As a result, we have obtained the
397 differences in terms of bias, sequence, and distribution across various seasons.

398 4. Results

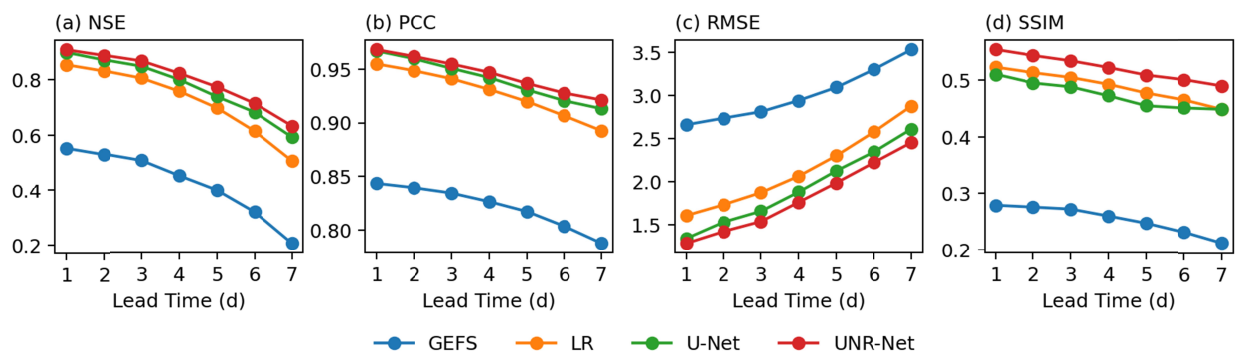
399 4.1 General downscaling performance

400 Figure 5 illustrates the error performance of the downscaled results from the three methods and
401 the low-resolution forecast data compared to the observations. the graph illustrates that the
402 downscaled results from the three methods exhibit significantly better performance in terms of
403 error compared to the low-resolution forecast data.

404 For NSE, PCC, and RMSE, the average differences between the LR method and U-Net over a
405 lead time from 1 to 7 days are 0.052, 0.013, and 0.220, respectively. In comparison, the
406 corresponding differences between the LR method and UNR-Net are 0.077, 0.016, and 0.338,
407 respectively. The LR method exhibits the poorest performance. As for the two deep learning
408 methods, their average differences are 0.025, 0.005, and 0.117, indicating a similar performance.
409 Moreover, as the lead time increases, the differences among the three methods become more

410 pronounced. When the lead time is 1 day, the gap between U-Net results and low-resolution data
 411 is 114% (NSE), 111% (PCC), and 125% (RMSE) compared to the gap between LR results and
 412 low-resolution data. Similarly, the gap between UNR-Net results and LR results is 117% (NSE),
 413 112% (PCC), and 131% (RMSE) compared to the gap with low-resolution data. When the lead
 414 time is 7 days, the gap between U-Net results and low-resolution data is 129% (NSE), 119%
 415 (PCC), and 141% (RMSE) compared to the gap between LR results and low-resolution data.
 416 Likewise, the gap between UNR-Net results and LR results is 142% (NSE), 127% (PCC), and
 417 165% (RMSE) compared to the gap with low-resolution data. UNR-Net demonstrates a greater
 418 advantage as the lead time becomes longer.

419 However, in the case of SSIM, the average score of U-Net is even lower than that of the LR
 420 method by 0.015. This indicates that U-Net performs worse than the LR method when
 421 considering SSIM. Indeed, the other three evaluation metrics (NSE, PCC, and RMSE)
 422 unequivocally attest to the superior calibration ability of U-Net compared to the LR method.
 423 However, the evaluation of SSIM measures the degree of structural similarity, which suggests
 424 that U-Net does not excel in the downscaling task. On the other hand, the modified network
 425 UNR-Net, when compared to the LR method, exhibits significant improvement. This implies that
 426 the checkerboard artifacts introduced by the transposed convolutions used in the upsampling
 427 process of U-Net diminish the practical application value of its results. Conversely, the modified
 428 UNR-Net incorporates a combination of nearest-neighbor interpolation and convolution. This
 429 approach successfully mitigates the issue of checkerboard artifacts, all the while maintaining
 430 unblemished result accuracy.



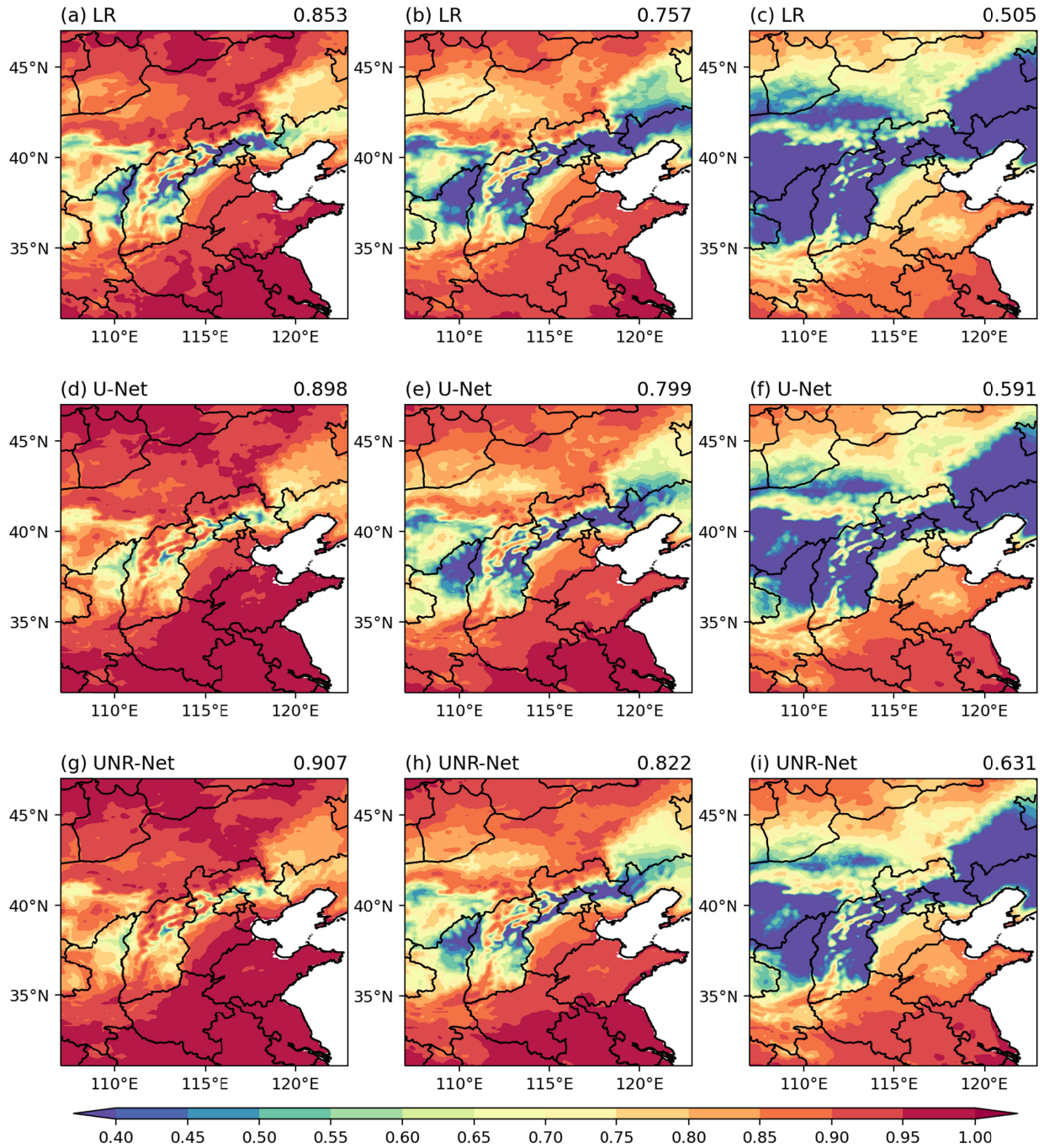
432 **Figure 5.** The overall evaluation of the three methods and the GEFS data. Variations in (a) NSE,
433 (b) PCC, (c) RMSE, and (d) SSIM of 2-m temperature at lead times of 1–7 days derived from the
434 GEFS, LR, U-Net, and UNR-Net averaged over North China.

435 The spatial distribution of NSE for the three methods is illustrated in Figure 6. Upon examining
436 the spatial distribution of the downscaled results from the three methods in fitting high-resolution
437 observational data, it becomes evident that the underperforming areas are concentrated around
438 the Taihang Mountain range. In certain regions, the scores even dip below 0.45. The scores
439 exhibit an increasing trend from both sides of the Taihang Mountain range in terms of spatial
440 distribution. Overall, there is a pattern of higher scores in the southeastern and northwestern
441 regions.

442 From LR to U-Net and then to UNR-Net, the fit of the predicted field to the observed field in the
443 region of the Taihang Mountains shows improvement. Moreover, within all lead times depicted
444 in the figure, the area characterized by scores below 0.45 exhibits a progressively diminishing
445 extent, with notable improvements observed, particularly in the vicinity of the Taihang
446 Mountains, for the two employed deep learning methodologies. Additionally, it is noteworthy
447 that the area encompassing scores exceeding 0.95 demonstrates a gradual increase in size. When
448 considering a lead time of 1 day, the distribution of regions with NSE scores below 0.45 for the
449 LR method is concentrated in the northeastern part of Shaanxi province and in the vicinity of the
450 Taihang Mountains. In fact, a majority of these areas even exhibit scores below 0.4. On the other
451 hand, regions with NSE scores surpassing 0.95 are mainly limited to Jiangsu, Anhui, Hubei, and
452 other areas. For the U-Net method, the extent of regions with NSE scores below 0.45 has been
453 significantly reduced. In the northeastern part of Shaanxi province, there are no longer any areas
454 with scores below 0.4. Furthermore, regions with NSE scores exceeding 0.95 now include
455 Shandong and Henan. As for the UNR-Net method, the area with NSE scores below 0.45 has
456 decreased compared to U-Net. In the northeastern part of Shaanxi province, southern Shanxi, and
457 Liaoning province, there are no longer any regions with scores below 0.45. The regions near the
458 Taihang Mountains with scores below 0.45 appear sporadically. Additionally, the region in the
459 southeast of Hebei province is now encompassed within the area with NSE scores surpassing
460 0.95, and the overall area in Shandong with scores below 0.95 has decreased compared to U-Net.
461 When considering lead times of 4 and 7 days, although the overall scores of all three methods

462 have decreased, certain patterns still emerge. The LR method exhibits the largest area with scores
463 below 0.45 and the smallest area with scores above 0.95. Conversely, UNR-Net showcases the
464 smallest area with scores below 0.45 and the largest area with scores above 0.95. Especially
465 noteworthy is the 7-day lead time, where the LR method has virtually no areas with scores above
466 0.95. In contrast, both deep learning methods still exhibit some distribution in the southeastern
467 region. Furthermore, the area with scores above 0.8 for UNR-Net is notably larger than that for
468 U-Net.

469 As the lead time increases, NSE scores progressively decrease. For instance, when comparing the
470 7-day lead time to the 1-day lead time, the LR method experiences a decrease of 0.348 in NSE,
471 while the U-Net method decreases by 0.307 and the UNR-Net method decreases by 0.276. It is
472 evident that UNR-Net exhibits a lower reduction magnitude compared to the other two methods.
473 Additionally, UNR-Net maintains a larger area with high NSE scores. Therefore, UNR-Net
474 demonstrates its superiority particularly in longer lead times, showcasing its favorable
475 performance.

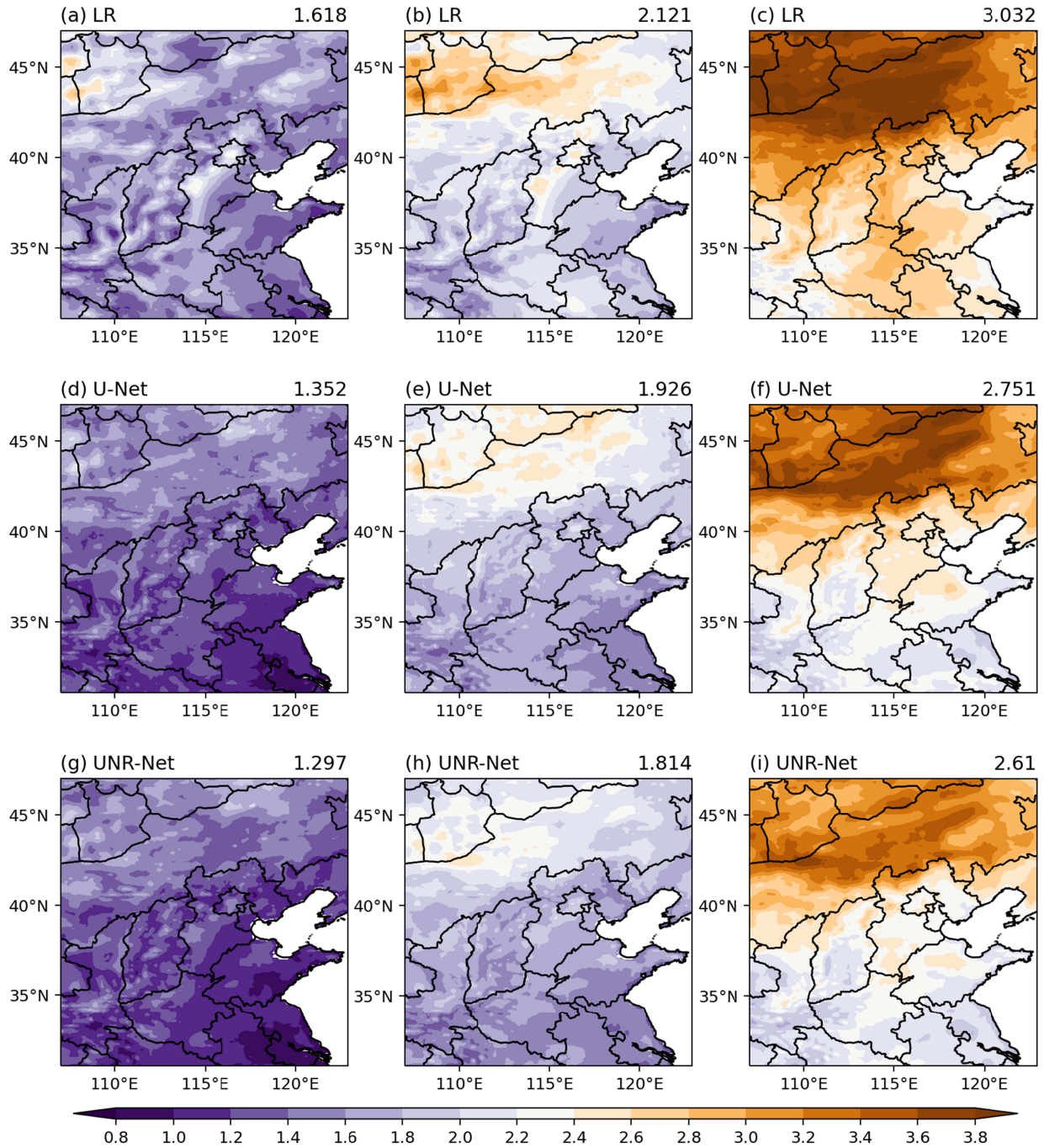


476

477 **Figure 6.** Spatial distributions of the NSE for 2-m temperature with lead times of 1, 4, and 7
 478 days derived from LR (a–c), U-Net (d–f), and UNR-net (g–i), the values in the upper-right title
 479 represent the mean of NSE in each case.

480 The spatial distribution of the root mean square error (RMSE) predominantly demonstrates a
 481 pattern of lower values in the southeast and higher values in the northwest (Figure 7).

482 Furthermore, as the lead time increases, the overall error tends to escalate. At a lead time of 1
483 day, the error distribution of the LR method appears to be relatively uniform. While the region
484 with errors below $0.6\text{ }^{\circ}\text{C}$ is predominantly concentrated in the eastern part, the overall
485 differences are not significant. On the other hand, U-Net and UNR-Net exhibit smaller errors in
486 the southeastern region, with large areas showing errors below $1.2\text{ }^{\circ}\text{C}$. Moreover, UNR-Net
487 showcases a larger region with errors below $1\text{ }^{\circ}\text{C}$ compared to U-Net. Specifically, UNR-Net
488 demonstrates a greater coverage of areas with errors below $1\text{ }^{\circ}\text{C}$ in Jiangsu, Anhui, and even in
489 Shandong, surpassing the performance of U-Net. Additionally, UNR-Net displays reduced errors
490 in regions with complex topography such as the Shandong Peninsula, Shaanxi, and Shanxi, with
491 a higher number of areas exhibiting errors below $1.2\text{ }^{\circ}\text{C}$. This highlights the stronger correction
492 capability of UNR-Net. At a lead time of 4 days, the LR method demonstrates an overall spatial
493 distribution pattern of lower errors in the eastern and western regions, with higher errors
494 observed in the central area. Specifically, there are areas in the central part of Hebei province
495 where errors exceed $2.2\text{ }^{\circ}\text{C}$, and some regions even exhibit errors surpassing $2.6\text{ }^{\circ}\text{C}$. In contrast,
496 the spatial distribution of the two deep learning methods does not exhibit a distinct pattern of
497 lower errors in the central region. Therefore, compared to the LR method, there is a significant
498 improvement in the central region, resulting in an overall pattern of lower errors in the southern
499 areas and higher errors in the northern areas. Notably, UNR-Net outperforms U-Net in terms of
500 the southern region, with a larger area showing errors below $1.6\text{ }^{\circ}\text{C}$. This is especially evident in
501 the complex terrain areas of southern Shaanxi and central Shanxi, where UNR-Net demonstrates
502 even lower errors, showcasing its superior downscaling capability in complex topography
503 conditions. At a lead time of 7 days, the error distribution of the LR method is similar to that at a
504 3-day lead time. Both deep learning methods also exhibit a pattern of higher errors in the
505 northern regions and lower errors in the southern regions. Additionally, UNR-Net exhibits lower
506 errors in the regions of Shandong and Hebei, showcasing its superior performance in those areas.
507 Moreover, UNR-Net demonstrates better downscaling capability in the southern regions of
508 Shaanxi and Shanxi as well.

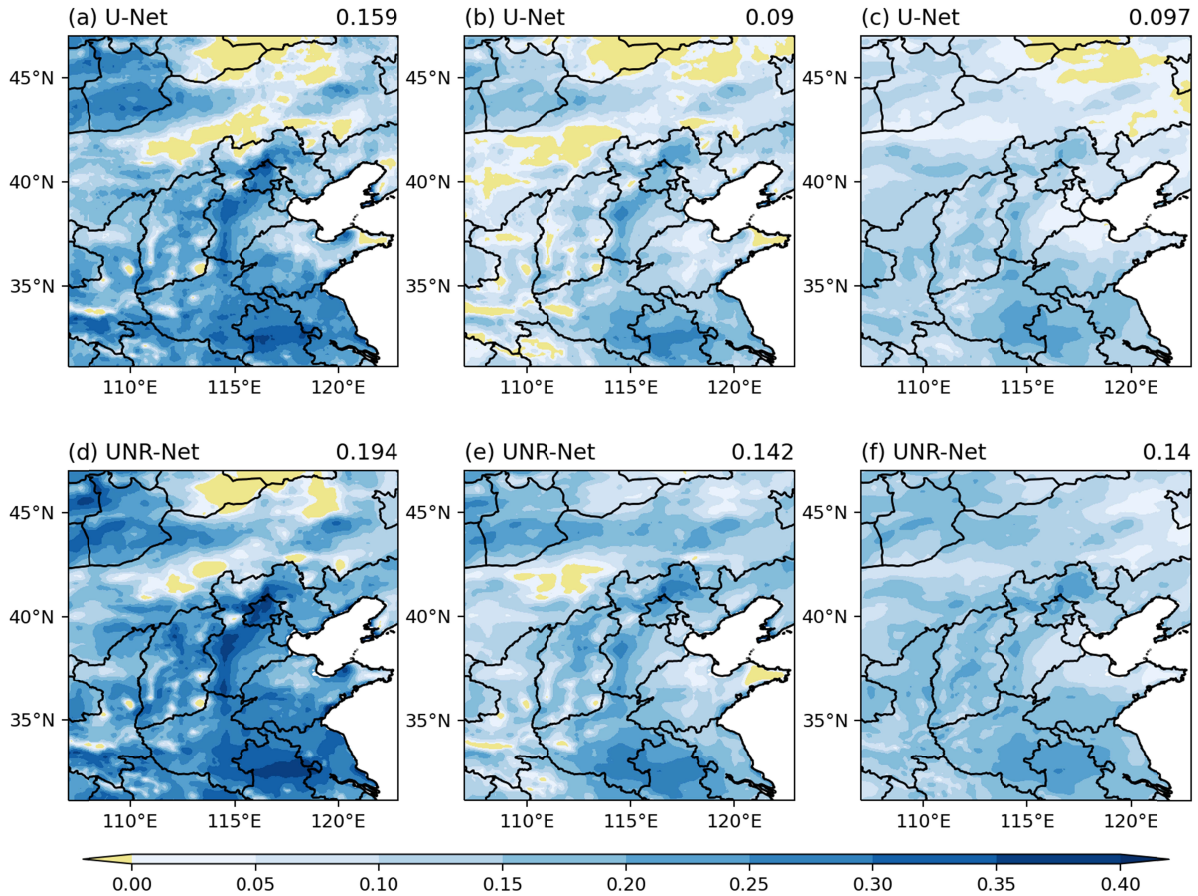


509

510 **Figure 7.** Spatial distributions of the RMSE for 2-m temperature with lead times of 1, 4, and 7
 511 days derived from LR (a–c), U-Net (d–f), and UNR-net (g–i) , the values in the upper-right title
 512 represent the mean of RMSE in each case.

513 Subsequently, a further comparison was made between the absolute error performance of the two
 514 deep learning methods (Figure 8). Overall, when comparing the improvement levels of the two

515 deep learning methods relative to the LR method, UNR-Net exhibits a greater degree of
516 improvement compared to U-Net. The RMSESS scores of UNR-Net, at lead times of 1, 4, and 7
517 days, were found to be higher than those of U-Net by 0.035, 0.052, and 0.043, respectively. It
518 can be observed that as the lead time increases, UNR-Net demonstrates a greater overall
519 improvement over the LR method. From the spatial distribution, it can be observed that the
520 significant improvements of both deep learning methods are concentrated in central Hebei,
521 Jiangsu, Anhui, and Henan. Across all lead times, these regions exhibit the lowest scores in the
522 entire area. At a lead time of 1 day, there are areas where the score is less than zero, indicating
523 minimal improvement compared to the LR method. These areas are mainly located in Inner
524 Mongolia, with UNR-Net exhibiting a smaller coverage compared to U-Net. In the Shandong
525 region, unlike U-Net, UNR-Net does not have any areas with scores less than 0. Comparing the
526 areas with higher scores, it can be observed that in central Hebei and Anhui, UNR-Net covers a
527 significantly larger area with scores above 0.3, and even areas with scores above 0.35, while U-
528 Net only has a small portion of the western Anhui region with scores above 0.35, and no such
529 distribution in other regions. The areas where significant improvements were observed are
530 primarily concentrated around the Taihang Mountains and the southeastern region. At lead times
531 of 4 and 7 days, the overall situation is similar to that at a lead time of 1 day. UNR-Net
532 outperforms U-Net in terms of higher scores. Particularly at a lead time of seven days, UNR-Net
533 shows improvements over the LR method in all regions. Thus, it further demonstrates the
534 superiority of UNR-Net, particularly at longer lead times.

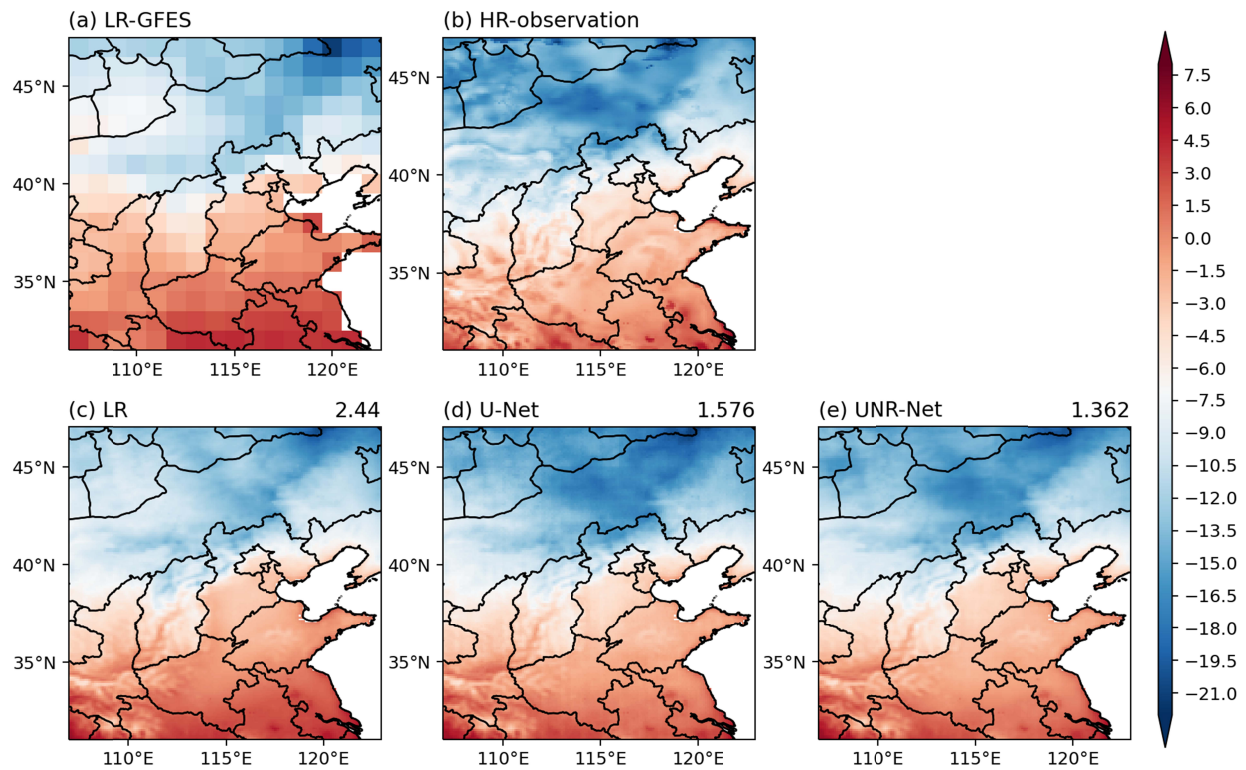


535

536 **Figure 8.** RMSESS spatial distribution of deep learning methods relative to LR methods for 2-m
 537 temperature with lead times of 1, 4, and 7 days derived from U-Net (a–c) and UNR-net (d–f) ,
 538 the values in the upper-right title represent the mean of RMSESS in each case.

539 Choosing a day from the testing dataset characterized by a widespread occurrence of low-
 540 temperature rain and snow events, we present three illustrative examples of downscaling
 541 methods (Figure 9). All three methods aim to downscale the low-resolution forecast data shown
 542 in Figure 12a to achieve results that closely resemble the high-resolution observational data
 543 depicted in Figure 12b. In this particular case, the forecast data generally exhibit lower values in
 544 the northern region compared to the observational data. This highlights the need for higher
 545 requirements in terms of correcting the forecast data. From the downscaling results of the three
 546 methods, it can be observed that all three methods exhibit finer textures compared to the low-
 547 resolution forecast data. In the case of the LR method, the blue color in the northern region
 548 appears lighter, indicating higher temperatures compared to the observed values and the
 549 downscaled results of the other two methods. Therefore, the LR method exhibits larger errors.

550 On the other hand, both deep learning methods show significantly smaller errors compared to the
 551 LR method, with UNR-Net demonstrating even smaller errors than U-Net.

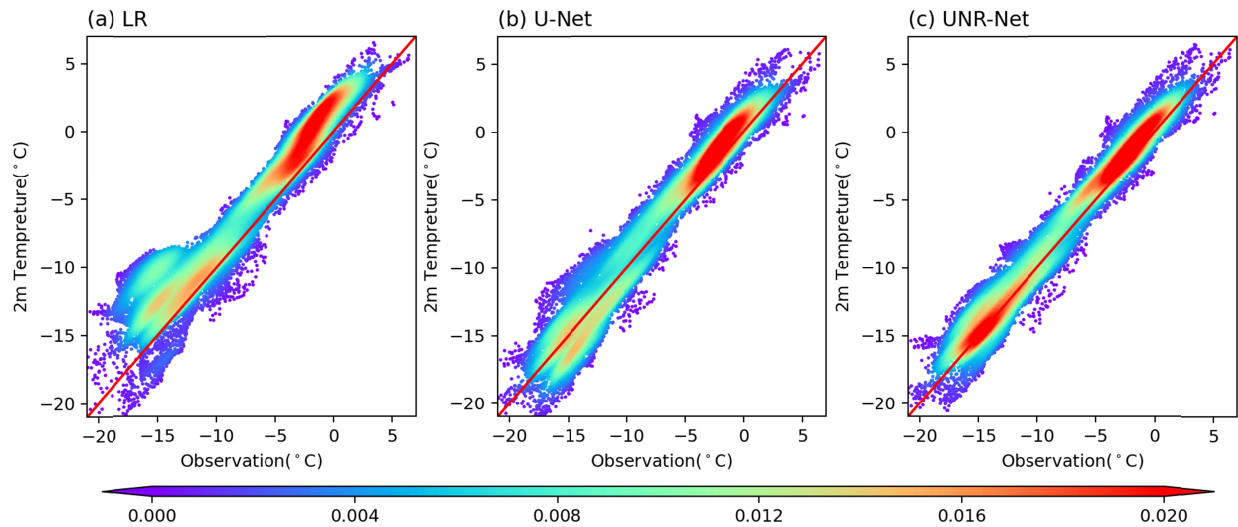


552

553 **Figure 9.** The 2-m temperature downscaling example for a lead time of 1 day on 6 December
 554 2019, with the (a) low-resolution forecast, (b) high-resolution observation, (c) LR downscaling
 555 result, (d) U-Net downscaling result and (e) UNR-Net downscaling result. The value in the
 556 upper-right title is the MSE of the three downscaled results.

557 The performance of a method in capturing extreme values is also an important criterion for
 558 assessing its effectiveness in the context of low-temperature rain and snow events. From Figure
 559 10, it is evident that for 6 December 2019, the downscaled results of the LR method consistently
 560 deviate from the red line. The values tend to be higher overall, indicating lower accuracy.
 561 Furthermore, the distribution of points appears to be widely scattered especially in the low-
 562 temperature range. The two deep learning methods exhibit significant improvements in accuracy
 563 compared to LR. The extent of deviation from the red line is reduced, and the points generally
 564 align along the line. Additionally, the distribution of points is much more concentrated compared
 565 to the LR method. For the two deep learning methods, UNR-Net demonstrates a better

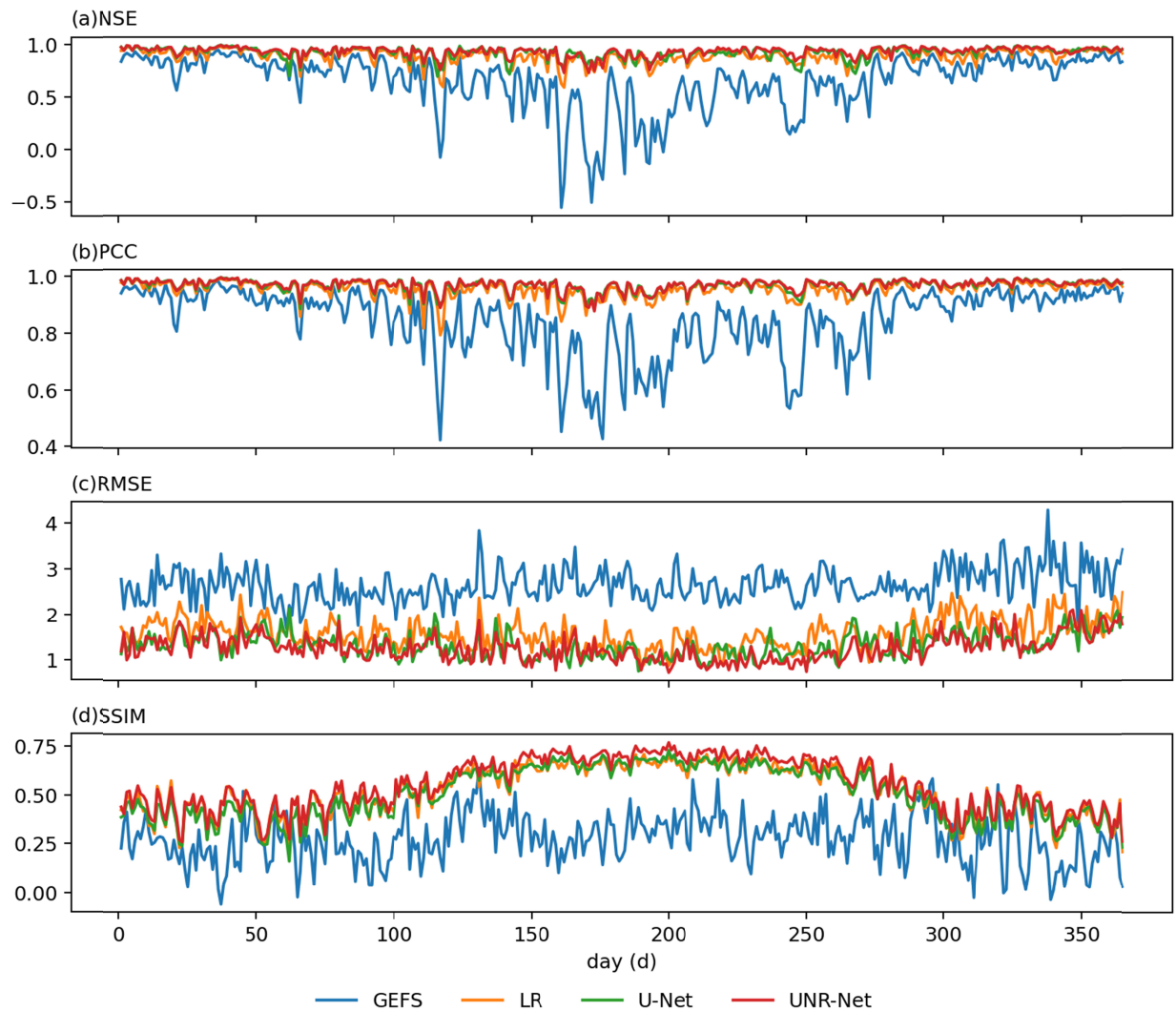
566 performance than U-Net in the low-temperature range. The points are more concentrated, with
 567 the distribution center aligning closely with the red line.



568
 569 **Figure 10.** Scatter plot density of the downscaled results for the three methods on 6 December
 570 2019, with a 24-h lead time derived from (a)LR, (b) U-Net, and (c) UNR-net.

571 As illustrated in the above example, for the majority of days in the testing dataset, the
 572 performance of the three methods is characterized by LR being the poorest and UNR-Net being
 573 the best (Figure 11). However, when considering the performance over the entire year in the
 574 testing dataset, noticeable seasonal variations can be observed. Regarding NSE and PCC, the
 575 performance of the low-resolution forecast data is not stable. It exhibits significant fluctuations
 576 and lower scores, particularly around the summer season. However, after downscaling using the
 577 three methods, the scores of the results remain stable throughout the year. This indicates a
 578 significant improvement in the fitting and correlation between the predicted and observed fields,
 579 particularly during the summer season. In terms of RMSE, although the error of the low-
 580 resolution forecast data fluctuates significantly at the beginning and end of the year and remains
 581 relatively constant throughout the middle of the year, the overall numerical value remains
 582 consistent. However, the error values of the downscaled results using the three methods do not
 583 exhibit a constant distribution. They generally show a pattern of being lower during the middle
 584 of the year and higher at the beginning and end of the year. However, the fluctuations are
 585 relatively evenly distributed throughout the year. In terms of SSIM, the low-resolution forecast
 586 data generally exhibits slightly higher scores during the middle of the year compared to the

587 beginning and end of the year, with less pronounced fluctuations. However, there are significant
 588 differences in the distribution of results for the three downscaled methods. The scores are
 589 noticeably higher and more stable during the middle of the year compared to the beginning and
 590 end of the year. Hence, it is necessary to conduct further analysis based on seasons to gain
 591 deeper insights.



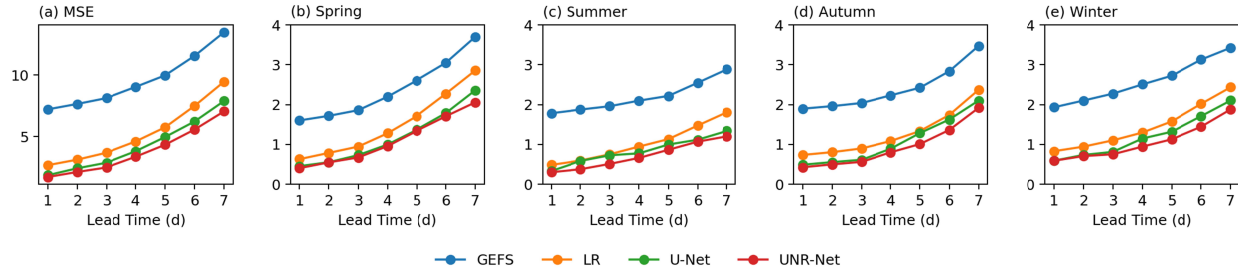
592

593 **Figure 11.** The error performance of the downscaled results for the three methods in the whole
 594 testing dataset and the GEFS data with a 1-d lead time for (a) NSE, (b) PCC, (c) RMSE, and (d)
 595 SSIM.

596 4.2 Error decomposition

597 The decomposition of MSE into four seasons (spring, summer, autumn, and winter) for lead
598 times of 1–7 days is illustrated in Figure 12. For the low-resolution forecast data, as the lead time
599 increases, the error also increases. However, the rate of increase is the smallest during the
600 summer season. The difference in error between a lead time of 7 days and 1 day is 1.10 in the
601 summer season, while it is 2.10 in the spring season, 1.58 in the autumn season, and 1.50 in the
602 winter season. Moreover, as the lead time increases, the error of the LR method becomes closer
603 to the error of the low-resolution forecast data in all four seasons. The difference between the
604 two decreases by 0.13, 0.22, 0.06, and 0.11 in the spring, summer, autumn, and winter seasons,
605 respectively, when comparing a lead time of 7 days to a lead time of 1 day. Particularly, the error
606 in the autumn and winter seasons shows a closer growth rate to that of the low-resolution
607 forecast data. As for the two deep learning methods, the difference between their errors and the
608 errors of the low-resolution forecast data changes differently compared to the performance of the
609 LR method as the lead time increases. For the U-Net method, the difference between the two
610 decreases by 0.035 and 0.017 in the autumn and winter seasons, respectively, when comparing a
611 lead time of 7 days to a lead time of 1 day. However, in the spring and summer seasons, the
612 difference increases by 0.20 and 0.10, respectively. On the other hand, for the UNR-Net method,
613 the difference between its error and the error of the low-resolution forecast data increases in all
614 four seasons as the lead time increases. The difference at a lead time of 7 days compared to a
615 lead time of 1 day increases by 0.45, 0.20, 0.08, and 0.20 in the spring, summer, autumn, and
616 winter seasons, respectively. This not only highlights the advantages of the two deep learning
617 methods, particularly UNR-Net, over the LR method but also further emphasizes that as the lead
618 time increases, the advantages of the deep learning methods, especially UNR-Net, become more
619 significant and comprehensive. Additionally, both deep learning methods demonstrate greater
620 advantages in the spring and summer seasons.

621



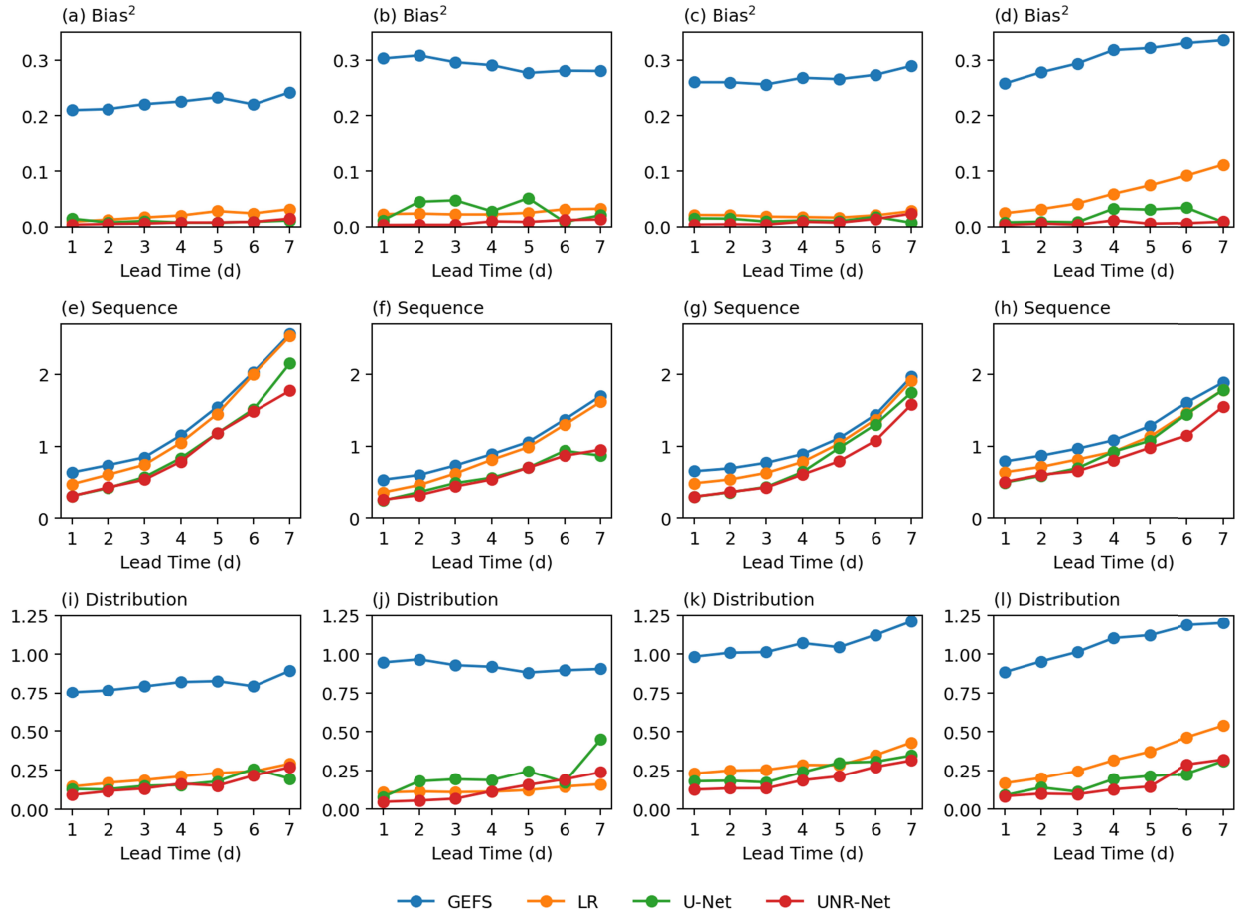
622

623 **Figure 12.** The decomposition of errors averaged over North China for each season across lead
 624 times of 1 to 7 days, with (a) MSE, (b) spring, (c) summer, (d) autumn, and (e) winter.

625 As shown in Figure 13, when decomposing the errors for the four seasons, it can be observed
 626 that the three downscaled methods exhibit significant improvements in the Bias and Distribution
 627 components. For the Bias term, the average values of the LR method across the four seasons are
 628 0.02, 0.03, 0.02, and 0.06, respectively. The average values of the U-Net method across the four
 629 seasons are 0.009, 0.03, 0.01, and 0.02, respectively. As for UNR-Net, the average values across
 630 the four seasons are 0.007, 0.007, 0.009, and 0.006, respectively. Indeed, it can be observed that
 631 UNR-Net has the smallest Bias term, with values below 0.01 in all four seasons. Particularly in
 632 the winter season, the difference between the LR method and the two deep learning methods is
 633 much more significant compared to the other three seasons. For the Distribution term, the
 634 average values of the LR method across the four seasons are 0.212, 0.124, 0.297, and 0.328,
 635 respectively. The average values of the U-Net method across the four seasons are 0.171, 0.215,
 636 0.246, and 0.182, respectively. As for UNR-Net, the average values across the four seasons are
 637 0.164, 0.124, 0.197, and 0.165, respectively. The patterns for the Distribution term are similar to
 638 those of the Bias term. UNR-Net consistently exhibits the lowest error, and in the winter season,
 639 the difference between the LR method and the two deep learning methods is significantly larger
 640 compared to the other three seasons.

641 As for the Sequence term, the LR method shows limited capability, especially at longer lead
 642 times, where the improvement relative to the low-resolution forecast data is minimal. At a lead
 643 time of 7 days, the difference between the low-resolution forecast and the LR method is only
 644 0.034, 0.083, 0.057, and 0.103 across the four seasons, respectively. On the other hand, at a lead
 645 time of 1 day, the difference between the two is 0.163, 0.177, 0.167, and 0.150 in the respective
 646 seasons. Clearly, as the lead time increases, the correction capability of the LR method becomes

647 weaker. Indeed, both deep learning methods demonstrate advantages over the LR method. The
648 discrepancies between the U-Net method and the low-resolution forecasts for the four seasons
649 are as follows: at a lead time of 1 day, they are 0.327, 0.289, 0.356, and 0.294, and at a lead time
650 of 7 days, they are 0.414, 0.832, 0.221, and 0.104. It can be observed that as the lead time
651 increases, the accuracy improvement of U-Net becomes more prominent during the spring and
652 summer seasons. The disparities between the UNR-Net method and the low-resolution forecasts
653 for the four seasons are as follows: at a lead time of 1 day, they are 0.329, 0.279, 0.354, and
654 0.284, and at a lead time of 7 days, they are 0.794, 0.748, 0.389, and 0.337. It can be observed
655 that as the lead time increases, the differences between the downscaled results of UNR-Net and
656 the low-resolution forecasts intensify across all four seasons. This indicates that the UNR-Net
657 method exhibits a greater degree of improvement over low-resolution forecasts with longer lead
658 times. This observation indicates that the Sequence component highlights the advantages of
659 nonlinear methods to a greater extent. Deep learning methods primarily improve the accuracy of
660 downscaling tasks in the temporal domain.



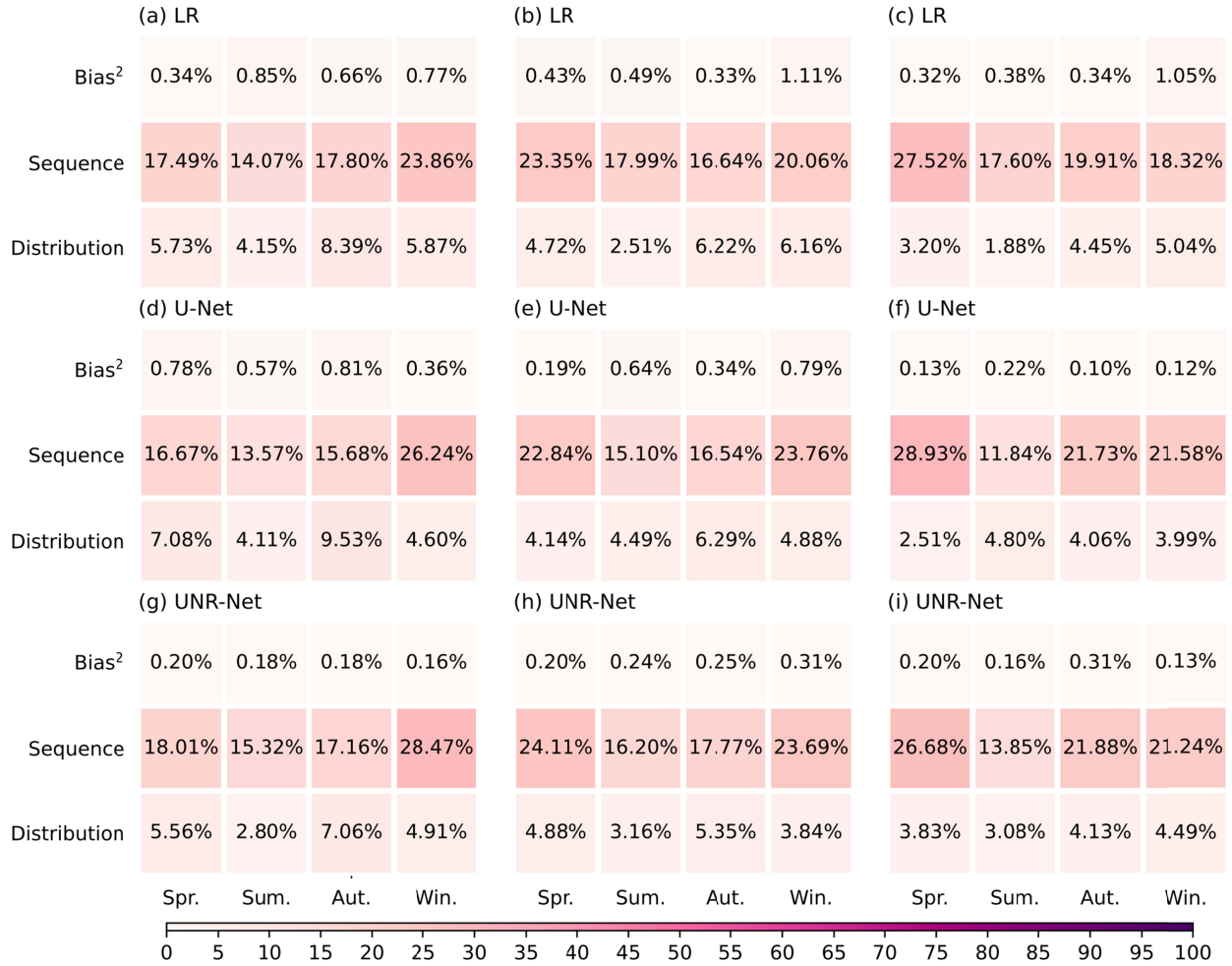
661

662 **Figure 13.** The values of Bias (a–d), Sequence (e–h), and Distribution (i–l) error components
 663 decomposed for lead times of 1 to 7 days for each season, (a, e, i) spring, (b, f, j) summer, (c, g,
 664 k) autumn, and (d, h, l) winter, averaged over North China.

665 The proportion of errors for each component after error decomposition is illustrated in Figure 14.
 666 For the errors associated with the Bias, Sequence, and Distribution components, Bias has the
 667 smallest proportion. The average proportions for the LR method, U-Net, and UNR-Net across the
 668 four seasons are 0.59%, 0.42%, and 0.21% for Bias, respectively. Next, is the Distribution
 669 component, with average proportions of 4.86%, 5.04%, and 4.43% for the LR method, U-Net,
 670 and UNR-Net across the four seasons, respectively. The dominant component is Sequence, with
 671 average proportions of 19.55%, 19.54%, and 20.36% for the LR method, U-Net, and UNR-Net
 672 across the four seasons, respectively. Therefore, the Sequence component plays a more
 673 significant role in determining the performance of the methods.

674 As the lead time increases, the proportion of the Sequence component gradually increases. For a
675 lead time of 1 day, the average proportions of the three methods across the four seasons are
676 18.30%, 18.04%, and 19.74% respectively. For a lead time of 4 days, the average proportions are
677 19.51%, 19.56%, and 20.44% respectively. For a lead time of 7 days, the average proportions are
678 20.84%, 21.02%, and 20.91% respectively. This trend may be attributed to the fact that the errors
679 in the forecast data in terms of temporal variability increase with longer lead times, resulting in a
680 higher proportion of temporal errors in the downscaled results of the three methods.

681 Furthermore, there have been changes in the proportions across seasons. For a lead time of 1 day,
682 the average proportions of the three methods across the four seasons are 7.98%, 6.17%, 8.59%,
683 and 10.58% respectively. It can be observed that the majority of errors are concentrated in the
684 winter season. When the lead time increases to 4 days, the average proportions across the four
685 seasons are 9.43%, 6.76%, 7.75%, and 9.40% respectively. For a lead time of 7 days, the average
686 proportions across the four seasons are 10.37%, 5.98%, 8.54%, and 8.44%, respectively. It can
687 be noted that with the increase in lead time, the seasons with higher proportions of errors
688 gradually shift toward the spring season.



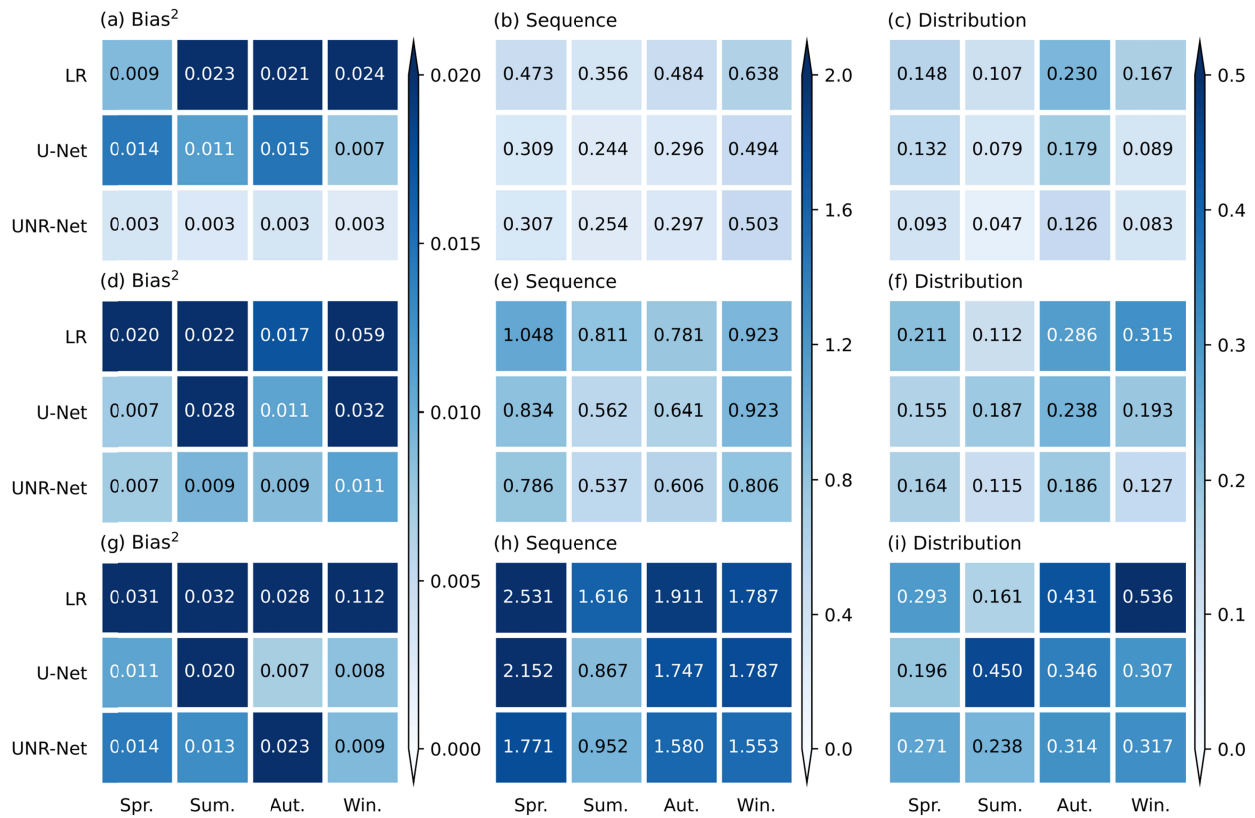
689

690 **Figure 14.** The decomposed 12 error components averaged over North China, represented as
 691 percentages with lead times of (a, d, g) 1, (b, e, h) 4, and (c, f, i) 7 days, derived from (a–c) LR,
 692 (d–f) U-Net, and (g–i) UNR-Net. The vertical axis represents errors for physical significance and
 693 the horizontal axis represents errors for the four seasons.

694 The numerical values for the decomposed error components are depicted in Figure 15. Based on
 695 the numerical values of the 12 error components, as the lead time increases, for lead times of 1,
 696 4, and 7 days, the average values of the Bias component for the three methods across the four
 697 seasons are 0.011, 0.019, and 0.013, respectively. The average values of the Sequence
 698 component are 0.388, 0.771, and 1.551, respectively. The average values of the Distribution
 699 component are 0.123, 0.191, and 0.305, respectively. It can be observed that the Sequence and
 700 Distribution components show significant increases, while the Bias component remains

701 relatively stable. Furthermore, across all components and lead times, U-Net outperforms LR, and
 702 UNR-Net outperforms U-Net.

703 For different seasons, the average values of the Bias component across the three lead times are
 704 0.013, 0.017, 0.014, and 0.030, respectively. Although the Bias component is almost twice as
 705 large in the winter season compared to the other three seasons, its contribution to the overall
 706 MSE is relatively small. Therefore, the winter season does not exhibit significantly higher errors
 707 compared to the other three seasons due to this component. The average values of the
 708 Distribution component across the three lead times are 0.185, 0.166, 0.260, and 0.237,
 709 respectively. The errors in the spring and summer seasons are smaller than the other two seasons.
 710 The average values of the Sequence component across the three lead times are 1.135, 0.689,
 711 0.927, and 1.046, respectively. The Sequence component exhibits much better performance in
 712 summer compared to the other three seasons. Moreover, the Sequence component has the highest
 713 values numerically, indicating its dominant role in MSE.



715 **Figure 15.** The decomposed error values of the 12 components averaged over North China with
716 lead times of (a–c) 1, (d–f) 4, and (g–i) 7 days. The vertical axis represents errors from three
717 different methods and the horizontal axis represents the seasonal error.

718 **5. Conclusions and discussion**

719 This paper introduces a novel downscaling network called UNR-Net, which integrates a non-
720 local attention mechanism, Res2net (Gao et al., 2019), and terrain information to further enhance
721 the accuracy and practical value of the results. A downscaling experiment with a downscaling
722 factor of 10x was conducted for the 2-m temperature forecast over the East China region at lead
723 times of 1–7 days. The LR and U-Net methods are conducted as benchmarks. To obtain a more
724 detailed and specific evaluation and enhance the interpretability of the models, the error
725 decomposition method based on MSE is also proposed.

726 Generally, the UNR-Net demonstrates superior performance over U-Net and LR methods in
727 terms of NSE, PCC, RMSE, and SSIM, particularly for longer lead times. Regarding NSE, PCC,
728 and RMSE, the LR method exhibits the poorest performance, followed by U-Net. The best-
729 performing method is UNR-Net. Both deep learning methods demonstrated a certain
730 improvement compared to the LR method when forecasting for longer lead times. Moreover,
731 UNR-Net exhibited a more pronounced enhancement compared to U-Net. For SSIM, the U-Net
732 method shows the poorest performance, followed by the LR method, while UNR-Net exhibits
733 the best performance. Therefore, it can be observed that UNR-Net has superior practical
734 applicability compared to U-Net. In terms of spatial distribution, the errors are primarily
735 concentrated in regions with complex terrain, such as the Taihang Mountains, Shanxi, central
736 Shaanxi, and Liaoning. UNR-Net exhibits significantly smaller errors in this area compared to
737 the other two methods, indicating its greater advantage in complex terrain regions. Furthermore,
738 it was observed that during the summer season, characterized by lower NSE and PCC values in
739 the low-resolution data, all three methods exhibited better performance in terms of RMSE and
740 SSIM.

741 Consequently, for a more in-depth analysis of the errors, the Mean Squared Error (MSE) is first
742 decomposed based on time into four seasons: spring, summer, autumn, and winter. Then, it is
743 further decomposed based on its physical significance into three components: Bias, Sequence,
744 and Distribution. Each method's error is decomposed into 12 constituent components. Indeed, it

745 can be observed that the three methods showed the lowest errors during the summer season.
746 Moreover, the deep learning methods, especially UNR-Net, displayed more significant
747 advantages as the lead time increased. Upon decomposing the errors for each season into Bias,
748 Sequence, and Distribution components, it can be observed that for the Bias and Distribution
749 components, all three methods showed significant improvements in downscaling results
750 compared to low-resolution data, with UNR-Net exhibiting the smallest error. Among the error
751 composition components, the Sequence component has the largest proportion and plays a
752 dominant role. Especially for longer lead times, the LR method showed little improvement
753 compared to low-resolution data, while both deep learning methods demonstrated higher
754 accuracy, with UNR-Net showing the smallest errors.

755 The success of UNR-Net in temperature downscaling highlights the feasibility of utilizing deep
756 learning methods and techniques such as non-local attention mechanisms and residual
757 connections for handling Earth system data. Although UNR-Net has already incorporated terrain
758 data, it lacks the utilization of additional meteorological variables. Existing studies have shown
759 that the integration of diverse meteorological variables can enhance the accuracy of results (Sun
760 & Tang, 2020; Harris et al., 2022). Therefore, in the future, it is worth considering the
761 incorporation of more meteorological elements into the downscaling task to further improve its
762 performance. On the other hand, with the ongoing advancements in deep learning technology,
763 there exists significant potential for further improvements in result accuracy and exploration of
764 new possibilities. Moreover, from an analysis of error decomposition, it is evident that the degree
765 of improvement varies for different error components. Therefore, in the future, it would be
766 beneficial to consider employing techniques tailored to specific physical meanings or seasons.
767 Incorporating approaches that target seasonality, mean values, temporal patterns, and
768 distributions, such as season-based transfer learning, holds the potential to not only enhance
769 overall error performance but also increase their practical value significantly.

770 **Acknowledgments**

771 This paper is supported by the National Natural Science Foundation of China (42275164) and the
772 Science and Technology Program of China Southern Power Grid Co., Ltd. (Grant No.
773 YNKJXM202222172), the Reserve Talents Program for Middle-aged and Young Leaders of

774 Disciplines in Science and Technology of Yunnan Province, China (Grant No.
775 202105AC160014). We are grateful to ECMWF and NCEP/NOAA for their datasets.

776 **Data Availability Statement**

777 Data related to this article are available free from Global Ensemble Forecasting System
778 (<https://noaa-gefs-retrospective.s3.amazonaws.com/index.html#GEFSv12/reforecast/>) (Guan et
779 al., 2020), ERA5-Land ([https://cds.climate.copernicus.eu/cdsapp#!/dataset/reanalysis-era5-
780 land?tab=form](https://cds.climate.copernicus.eu/cdsapp#!/dataset/reanalysis-era5-land?tab=form)) (Muñoz-Sabater et al, 2021) and ETOPO1 ([https://www.ngdc.noaa.gov/thredds
781 /catalog/global/ETOPO2022/60s/60s_bed_elev_netcdf/catalog.html?dataset=globalDatasetScan/
782 ETOPO2022/60s/60s_bed_elev_netcdf/ETOPO_2022_v1_60s_N90W180_bed.nc](https://www.ngdc.noaa.gov/thredds/catalog/global/ETOPO2022/60s/60s_bed_elev_netcdf/catalog.html?dataset=globalDatasetScan/ETOPO2022/60s/60s_bed_elev_netcdf/ETOPO_2022_v1_60s_N90W180_bed.nc)) (Amante &
783 Eakins, 2009). These data have been processed with Python (version 3.8.8). The training process
784 was executed using NVIDIA RTX A5000 under PyTorch1.11, which can be accessed from
785 <https://pytorch.org/>.

786 **References**

- 787 Amante, C., & Eakins, B. (2009). ETOPO1 arc-minute global relief model: Procedures, data
788 sources and analysis [Dataset]. *NOAA Tech. Memo*, NESDIS NGDC-24, 25 pp.
- 789 Baño-Medina, J., Manzananas, R., & Gutiérrez, J. M. (2020). Configuration and intercomparison of
790 deep learning neural models for statistical downscaling. *Geoscientific Model Development*,
791 *13*(4), 2109–2124.
- 792 Chen, J., Chen, H., & Guo, S. (2018). Multi-site precipitation downscaling using a stochastic
793 weather generator. *Climate Dynamics*, *50*, 1975–1992.
- 794 Dong, C., Loy, C. C., He, K., & Tang, X. (2015). Image super-resolution using deep
795 convolutional networks. *IEEE Transactions on Pattern Analysis and Machine Intelligence*,
796 *38*(2), 295–307.

- 797 Doury, A., Somot, S., Gadat, S., Ribes, A., & Corre, L. (2023). Regional Climate Model
798 emulator based on deep learning: concept and first evaluation of a novel hybrid downscaling
799 approach. *Climate Dynamics*, 60(56), 1751–1779.
- 800 Dumoulin, V., Belghazi, I., Poole, B., Mastropietro, O., Lamb, A., Arjovsky, M., & Courville, A.
801 (2016). Adversarially learned inference. *arXiv preprint arXiv:1606.00704*.
- 802 Feser, F., Rockel, B., von Storch, H., Winterfeldt, J., & Zahn, M. (2011). Regional climate
803 models add value to global model data: a review and selected examples. *Bulletin of the American*
804 *Meteorological Society*, 92(9), 1181–1192.
- 805 Fowler, H. J., Blenkinsop, S., & Tebaldi, C. (2007). Linking climate change modelling to
806 impacts studies: recent advances in downscaling techniques for hydrological modelling.
807 *International Journal of Climatology: A Journal of the Royal Meteorological Society*, 27(12),
808 1547–1578.
- 809 Frei, C., Christensen, J. H., Déqué, M., Jacob, D., Jones, R. G., & Vidale, P. L. (2003). Daily
810 precipitation statistics in regional climate models: Evaluation and intercomparison for the
811 European Alps. *Journal of Geophysical Research: Atmospheres*, 108(D3).
- 812 Gao, S. H., Cheng, M. M., Zhao, K., Zhang, X. Y., Yang, M. H., & Torr, P. (2019). Res2net: A
813 new multi-scale backbone architecture. *IEEE transactions on pattern analysis and machine*
814 *intelligence*, 43(2), 652–662.
- 815 Gauthier, J. (2014). Conditional generative adversarial nets for convolutional face generation.
816 *Class project for Stanford CS231N: convolutional neural networks for visual recognition, Winter*
817 *semester, 2014(5)*, 2.
- 818 Gerges, F., Boufadel, M. C., Bou-Zeid, E., Nassif, H., & Wang, J. T. (2022, January). A novel
819 deep learning approach to the statistical downscaling of temperatures for monitoring climate

820 change. In *2022 The 6th International Conference on Machine Learning and Soft Computing*
821 (pp. 1–7).

822 Guan H, Zhu Y, Sinsky E, et al. (2020). The NCEP GEFS-v12 reforecasts to support subseasonal
823 and hydrometeorological applications [Dataset]. In *Climate Prediction S&T Digest, 44rd NOAA*
824 *Climate Diagnostics and Prediction Workshop special issue*.

825 Hagemann, S., Machenhauer, B., Jones, R., Christensen, O. B., Déqué, M., Jacob, D., & Vidale,
826 P. L. (2004). Evaluation of water and energy budgets in regional climate models applied over
827 Europe. *Climate Dynamics*, 23, 547–567.

828 Han L, Chen M, Chen K, et al. (2021). A deep learning method for bias correction of ECMWF
829 24–240 h forecasts. *Advances in Atmospheric Sciences*, 38(9), 1444–1459.

830 Harris, L., McRae, A. T., Chantry, M., Dueben, P. D., & Palmer, T. N. (2022). A generative deep
831 learning approach to stochastic downscaling of precipitation forecasts. *Journal of Advances in*
832 *Modeling Earth Systems*, 14(10), e2022MS003120.

833 He, K., Zhang, X., Ren, S., & Sun, J. (2016a). Deep residual learning for image recognition. In
834 *Proceedings of the IEEE conference on computer vision and pattern recognition* (pp. 770–778).

835 He, X., Chaney, N. W., Schleiss, M., & Sheffield, J. (2016b). Spatial downscaling of
836 precipitation using adaptable random forests. *Water Resources Research*, 52(10), 8217–8237.

837 Hodson, T. O., Over, T. M., & Foks, S. S. (2021). Mean squared error, deconstructed. *Journal of*
838 *Advances in Modeling Earth Systems*, 13(12), e2021MS002681.

839 Höhle, K., Kern, M., Hewson, T., & Westermann, R. (2020). A comparative study of
840 convolutional neural network models for wind field downscaling. *Meteorological Applications*,
841 27(6), e1961.

- 842 Hu, J., Shen, L., & Sun, G. (2018). Squeeze-and-excitation networks. In *Proceedings of the IEEE*
843 *conference on computer vision and pattern recognition* (pp. 7132–7141).
- 844 Huang, G., Liu, Z., Van Der Maaten, L., & Weinberger, K. Q. (2017). Densely connected
845 convolutional networks. In *Proceedings of the IEEE conference on computer vision and pattern*
846 *recognition* (pp. 4700–4708).
- 847 Ioffe, S., & Szegedy, C. (2015, June). Batch normalization: Accelerating deep network training
848 by reducing internal covariate shift. In *International conference on machine learning* (pp. 448–
849 456). pmlr.
- 850 Ji, Y., Gong, B., Langguth, M., Mozaffari, A., & Zhi, X. (2022). CLGAN: A GAN-based video
851 prediction model for precipitation nowcasting. *EGUsphere*, 1–23.
- 852 Ji, L., Zhi, X., Schalge, B., Stephan, K., Wu, Z., Wu, C., ... & Zhu, S. (2023a). Dynamic
853 downscaling ensemble forecast of an extreme rainstorm event in South China by COSMO EPS.
854 *AI-based prediction of high-impact weather and climate extremes under global warming: A*
855 *perspective from the large-scale circulations and teleconnections*, 16648714, 143.
- 856 Ji, Y., Zhi, X., Ji, L., Zhang, Y., Hao, C., & Peng, T. (2023b). Deep-learning-based. *AI-based*
857 *prediction of high-impact weather and climate extremes under global warming: A perspective*
858 *from the large-scale circulations and teleconnections*, 16648714, 200.
- 859 Jing, Y., Lin, L., Li, X., Li, T., & Shen, H. (2022). An attention mechanism based convolutional
860 network for satellite precipitation downscaling over China. *Journal of Hydrology*, 613, 128388.
- 861 Jones, P. W. (1999). First-and second-order conservative remapping schemes for grids in
862 spherical coordinates. *Monthly Weather Review*, 127(9), 2204–2210.

- 863 Kim, G., & Barros, A. P. (2002). Downscaling of remotely sensed soil moisture with a modified
864 fractal interpolation method using contraction mapping and ancillary data. *Remote Sensing of*
865 *Environment*, 83(3), 400–413.
- 866 Kingma, D. P., & Ba, J. (2014). Adam: A method for stochastic optimization. *arXiv preprint*
867 *arXiv:1412.6980*.
- 868 Kumar, B., Chattopadhyay, R., Singh, M., Chaudhari, N., Kodari, K., & Barve, A. (2021). Deep
869 learning-based downscaling of summer monsoon rainfall data over Indian region. *Theoretical*
870 *and Applied Climatology*, 143, 1145–1156.
- 871 Li, X., Chen, S., Hu, X., & Yang, J. (2019). Understanding the disharmony between dropout and
872 batch normalization by variance shift. In *Proceedings of the IEEE/CVF conference on computer*
873 *vision and pattern recognition* (pp. 2682–2690).
- 874 Mannig B, Müller M, Starke E, et al. (2013). Dynamical downscaling of climate change in
875 Central Asia. *Global and Planetary Change*, 110, 26–39.
- 876 Mnih, V., Heess, N., & Graves, A. (2014). Recurrent models of visual attention. *Advances in*
877 *Neural Information Processing Systems*, 27.
- 878 Muñoz-Sabater J, Dutra E, Agustí-Panareda A, et al. (2021). ERA5-Land: A state-of-the-art
879 global reanalysis dataset for land applications [Dataset]. *Earth system science data*, 13(9), 4349-
880 4383.
- 881 Nash, J. E., & Sutcliffe, J. V. (1970). River flow forecasting through conceptual models part I—
882 A discussion of principles. *Journal of Hydrology*, 10(3), 282–290.
- 883 Pan, B., Hsu, K., AghaKouchak, A., & Sorooshian, S. (2019). Improving precipitation estimation
884 using convolutional neural network. *Water Resources Research*, 55(3), 2301–2321.

- 885 Park, S., Singh, K., Nellikkattil, A., Zeller, E., Mai, T. D., & Cha, M. (2022, August).
886 Downscaling Earth System Models with Deep Learning. In *Proceedings of the 28th ACM*
887 *SIGKDD Conference on Knowledge Discovery and Data Mining* (pp. 3733–3742).
- 888 Rind, D., Rosenzweig, C., & Goldberg, R. (1992). Modelling the hydrological cycle in
889 assessments of climate change. *Nature*, *358*(6382), 119–122.
- 890 Roberts, C. D., Senan, R., Molteni, F., Boussetta, S., Mayer, M., & Keeley, S. P. (2018). Climate
891 model configurations of the ECMWF Integrated Forecasting System (ECMWF-IFS cycle 43r1)
892 for HighResMIP. *Geoscientific Model Development*, *11*(9), 3681–3712.
- 893 Ronneberger, O., Fischer, P., & Brox, T. (2015). U-net: Convolutional networks for biomedical
894 image segmentation. In *Medical Image Computing and Computer-Assisted Intervention—*
895 *MICCAI 2015: 18th International Conference, Munich, Germany, October 5-9, 2015,*
896 *Proceedings, Part III 18* (pp. 234–241).
- 897 Sha, Y., Gagne II, D. J., West, G., & Stull, R. (2020). Deep-learning-based gridded downscaling
898 of surface meteorological variables in complex terrain. Part I: Daily maximum and minimum 2-
899 m temperature. *Journal of Applied Meteorology and Climatology*, *59*(12), 2057–2073.
- 900 Sharifi, E., Saghafian, B., & Steinacker, R. (2019). Downscaling satellite precipitation estimates
901 with multiple linear regression, artificial neural networks, and spline interpolation techniques.
902 *Journal of Geophysical Research: Atmospheres*, *124*(2), 789–805.
- 903 Silver, D., Schrittwieser, J., Simonyan, K., Antonoglou, I., Huang, A., Guez, A., ... & Hassabis,
904 D. (2017). Mastering the game of go without human knowledge. *Nature*, *550*(7676), 354–359.
- 905 Srivastava, N., Hinton, G., Krizhevsky, A., Sutskever, I., & Salakhutdinov, R. (2014). Dropout: a
906 simple way to prevent neural networks from overfitting. *The Journal Of Machine Learning*
907 *Research*, *15*(1), 1929–1958.

- 908 Sun, A. Y., & Tang, G. (2020). Downscaling satellite and reanalysis precipitation products using
909 attention-based deep convolutional neural nets. *Frontiers in Water*, 2, 536743.
- 910 Vandal, T., Kodra, E., & Ganguly, A. R. (2019). Intercomparison of machine learning methods
911 for statistical downscaling: the case of daily and extreme precipitation. *Theoretical and Applied
912 Climatology*, 137, 557–570.
- 913 Veit, A., Wilber, M. J., & Belongie, S. (2016). Residual networks behave like ensembles of
914 relatively shallow networks. *Advances in Neural Information Processing Systems*, 29.
- 915 Wang, X., Girshick, R., Gupta, A., & He, K. (2018). Non-local neural networks. In *Proceedings
916 of the IEEE conference on computer vision and pattern recognition* (pp. 7794–7803).
- 917 Wang, F., Tian, D., Lowe, L., Kalin, L., & Lehrter, J. (2021). Deep learning for daily
918 precipitation and temperature downscaling. *Water Resources Research*, 57(4), e2020WR029308.
- 919 Wilby, R. L., & Wigley, T. M. (1997). Downscaling general circulation model output: a review
920 of methods and limitations. *Progress in Physical Geography*, 21(4), 530–548.
- 921 Wilby, R. L., Wigley, T. M. L., Conway, D., Jones, P. D., Hewitson, B. C., Main, J., & Wilks, D.
922 S. (1998). Statistical downscaling of general circulation model output: A comparison of methods.
923 *Water Resources Research*, 34(11), 2995–3008.
- 924 Woo, S., Park, J., Lee, J. Y., & Kweon, I. S. (2018). Cbam: Convolutional block attention
925 module. In *Proceedings of the European conference on computer vision (ECCV)* (pp. 3–19).
- 926 Xie, S., Girshick, R., Dollár, P., Tu, Z., & He, K. (2017). Aggregated residual transformations
927 for deep neural networks. In *Proceedings of the IEEE conference on computer vision and pattern
928 recognition* (pp. 1492–1500).

- 929 Yuan, Q., Shen, H., Li, T., Li, Z., Li, S., Jiang, Y., ... & Zhang, L. (2020). Deep learning in
930 environmental remote sensing: Achievements and challenges. *Remote Sensing of Environment*,
931 *241*, 111716.
- 932 Zhu, Y., Zhi, X., Lyu, Y., Zhu, S., Tong, H., Ali, M., ... & Huo, W. (2022). Forecast
933 Calibrations of Surface Air Temperature over Xinjiang Based on U-net Neural Network.
934 *Frontiers in Environmental Science*, 1826.